Shakedown limit analysis of railway slab track foundations under train loading

Tengfei Wang

School of Civil Engineering, Southwest Jiaotong University, Chengdu 610031, China
MOE Key Laboratory of High-Speed Railway Engineering, Southwest Jiaotong University, Chengdu 610031, China
ORCID: 0000-0003-4079-0687
Email: w@swjtu.edu.cn

David P. Connolly

School of Civil Engineering, University of Leeds, Leeds LS2 9JT, UK
Email: D.Connolly@leeds.ac.uk

Qiang Luo

School of Civil Engineering, Southwest Jiaotong University, Chengdu 610031, China
MOE Key Laboratory of High-Speed Railway Engineering, Southwest Jiaotong University, Chengdu 610031, China
Email: lqrock@swjtu.edu.cn

Qingzhi Ye*

School of Civil Engineering, Southwest Jiaotong University, Chengdu 610031, China
Email: qingzhiye@my.swjtu.edu.cn (*Corresponding author)

Kaiwen Liu

School of Civil Engineering, Southwest Jiaotong University, Chengdu 610031, China
MOE Key Laboratory of High-Speed Railway Engineering, Southwest Jiaotong University, Chengdu 610031, China
Email: kaiwen.liu@queensu.ca

Abstract

Shakedown limit analysis is used to calculate the factor of safety of a structure subject to cyclic moving loading. It is a promising approach for railway slab track structural design because it can help identify the required layer thicknesses and material strength properties. However, the approach is based on an underlying assumption that the stress field in the train passage direction is invariant, which is violated for slab tracks in the vicinity of expansion joints. To address this issue, this paper proposes a novel shakedown limit analysis implementation that enables its use for slab tracks with joints. Firstly, a 3D finite element slab track model is developed to calculate the stress field profiles exerted on the subgrade surface. Analytical equations describing the shape of these profiles are then derived, considering locations along the slab track, including those near and far from expansion joints. Relationships are also derived to describe the stress field profile variation with depth, including both train-induced and geostatic stresses. Next, a lower-bound shakedown limit method is used to calculate the elastic shakedown limit based on the Mohr-Coulomb criterion using the computed stress fields. After the model is validated, shakedown limits are examined, considering various friction angles, cohesions, and Poisson's ratios. It is shown that the limit is reduced when the geostatic stresses in the ground are ignored. Furthermore, the shakedown limit is not always directly proportional to subsoil cohesion and increases with Poisson's ratio.

Keywords: shakedown limit; railway slab track; track expansion joints; railway geostatic stress; subgrade surface stress

1. Introduction

Slab tracks are extensively used in railway engineering as they offer the stable and level foundation necessary for a safe and comfortable journey (Wang et al. 2020). To evaluate the performance of a track substructure design, residual stresses resulting from cyclic moving loading caused by traffic must be taken into account. It is crucial to establish an acceptable load threshold that ensures a stable track substructure over a considerable number of load cycles. Failure to do so can lead to the gradual development of plastic strains in the track substructure, ultimately resulting in fatigue failure.

Shakedown limit analysis is an approach for determining the maximum permissible load for structures exposed to cyclic moving loads (Connolly et al. 2020). It considers failure modes such as the accumulation of excessive plastic strains, fatigue, and instantaneous collapse. In contrast to numerical elastoplastic analysis, shakedown analysis is a more straightforward method that predicts the long-term behavior of structures subjected to a large number of load cycles by exploring the most critical point throughout the elastoplastic structure. Furthermore, it does not require time-stepping calculations, making it a computationally efficient approach.

The concept of shakedown was first introduced by Bleich (1932), Melan (1938), and Koiter (1960) in their works exploring the long-term response of elastoplastic structures to cyclic or moving loads. When the load level is above the yield limit but below the elastic shakedown limit, the structure will initially undergo plastic deformation, adapt to the load over time, and ultimately exhibit elastic behavior. However, if the load level exceeds the elastic shakedown limit, the structure will experience plastic deformation at every load cycle, leading to excessive permanent deformation or alternate plasticity and eventual failure.

Classical shakedown theory gave rise to the lower bound theorem (Boulbibane and Weichert 1997; Sharp and Booker 1984; Raad, Weichert, and Najm 1988; Yu and Hossain 1998) and the upper bound theorem (Collins and Boulbibane 2000; Collins and Cliffe 1987; Ponter, Hearle, and Johnson

1985), developed to determine the shakedown limit load of structures. The former provides a conservative solution, while the latter offers a less conservative solution. Although initial approaches were limited to 2D problems, shakedown analysis has also been expanded to encompass 3D problems (Yu 2005). It has received considerable attention in the fields of pavement (Collins, Wang, and Saunders 1993; Connolly and Yu 2020; Krabbenhøft, Lyamin, and Sloan 2007; Zhao et al. 2008; Zhuang and Wang 2018; Wang and Yu 2014; Li and Zhang 2010; Wang and Yu 2013a) and, more recently, in railway engineering (Liu et al. 2018; Wang et al. 2020; Wang and Yu 2021; Alves Costa, Lopes, and Silva Cardoso 2018; Zhuang 2020; Wang, Liu, and Yang 2018; Bi et al. 2022). It can be utilized to calculate factors of safety and optimize design layer thicknesses.

Shakedown analysis in railway engineering requires careful consideration of the track structure and its transmission of loading to the subsoil/trackbed surface. Despite recent advancements, the application of shakedown analysis in railway engineering remains limited. Previous studies utilized the shakedown lower bound theorem to determine shakedown limits of ballasted railways (Zhuang 2020; Zhuang et al. 2019; Wang and Zhuang 2021) and slab tracks (Wang and Yu 2021; Wang, Liu, and Yang 2018), establishing a relationship between dynamic shakedown limits and critical speeds for high-speed railways. Liu et al. (2018) studied the effects of depth-dependent stiffness modulus on shakedown limits, while Costa et al. (2018) examined the impact of train geometry, track stiffness, and soil improvement on a slab track system, accounting for geostatic stresses in the ground using a 2.5D approach. However, due to the presence of track expansion joints, the stress on the subsoil surface for typical slab tracks used in high-speed railways differs from general track structure positions (Ye et al. 2023). Therefore, a comprehensive shakedown analysis of slab track structures should also consider the impact of this structural discontinuity.

To address the impact of track expansion joints on shakedown limit analysis for railway slab track structures, this paper aims to simulate the shakedown behavior of slab track structures with discontinuities, subject to moving loads. First a 3D dynamic finite element model is developed to determine the load pattern and stress peaks on the trackbed at differing positions related to the expansion joints. Analytical equations are developed based upon load position to define the upper and lower bounds of the stress fields. Then a parametric study investigates how the subsoil's material properties affect the shakedown limit load. Additionally, the study incorporates shakedown analysis into the design process by determining the lower and upper bounds of the equivalent axle load for different operating speeds.

2. Analytical shakedown solution

This section introduces the general lower-bound shakedown theorems and shakedown computation procedure.

2.1 Lower-bound shakedown theorems

When a highway or railway is subjected to a moving load, it can experience both elastic and plastic deformation. Shakedown refers to the phenomenon where a material, initially undergoing permanent deformation due to repeated loads exceeding its elastic limit, eventually returns to elastic behavior after a finite number of cycles, as long as the load is below the elastic shakedown load limit. Thus, plastic deformation accumulation does not persist indefinitely for all load magnitudes surpassing the elastic limit. After each load cycle, residual stresses, in addition to plastic strains, remain, resulting in the total stress field being the sum of the residual stress from previous cycles and the applied load. Radovsky and Murashina (1996) observed experimentally the permanence of residual horizontal stresses on pavements after the passage of moving loads, while Wang and Yu (2013b) reached similar conclusions through numerical analysis of the shakedown problem.

A key consideration is whether the load exceeds the shakedown load limit. If the load exceeds this limit, a shakedown state will not occur. Instead, the permanent strains may settle into a closed cycle, which is called "cyclic" or "alternating plasticity," or they may continuously increase, a phenomenon known as "ratcheting." In either scenario, the structure will eventually fail (Collins and Boulbibane 2000).

Melan's lower-bound shakedown theorem (Melan 1938) has been employed to determine the shakedown limit of a continuous earth structure, which emphasizes the importance of establishing a critical residual stress field. For a structure subject to moving train loads, assuming uniform settlement in the half-space after a large number of load cycles (Yu 2005), the induced residual stress should be equilibrated and time-independent, as each point located at the cross-section perpendicular to the travel direction undergoes the same load history. In other words, shakedown will occur if the following condition is satisfied for any time and location of the body under analysis:

$$f(\lambda\sigma_{ij}^{e} + \sigma_{ij}^{0} + \sigma_{ij}^{r}) \leq 0 \tag{1}$$

where $f(\cdot)$ represents the yielding criteria; $\lambda\sigma_{ij}^{e}$ is the elastic stress field due to the applied load, λ is a load factor of the stress field generated by a fundamental loading scenario; the subscripts i and j define the coordinate inside the plane of the half-space under consideration, where i is the vertical direction and j is the direction of load movement; σ_{ij}^{0} is the static stress induced by the structure's self-weight.

2.2 Shakedown analysis

As highlighted by (Yu 2005; Yu and Wang 2012), the largest value of λ obtained by searching all possible self-equilibrated residual stress fields will give the actual shakedown limit $P_{\mathrm{sd}} = \lambda_{\mathrm{sd}} \cdot P$. Therefore, the aim is to find a residual stress state that is compatible with the restrictions expressed above: it needs to be self-equilibrated, time independent and its conjunction with the geostatic stress state must give rise to a total stress state that does not violate the yielding criteria.

To obtain a time-independent residual stress field, it is necessary to define a critical plane that is independent of the longitudinal direction. Yu (2005) and more recently Yu and Wang (2012) have shown that for a moving three-dimensional Hertz pressure distribution, the critical plane should be defined by y = constant (y-direction is the horizontal direction normal to the direction of movement), with the plane $y = 0$ being the most critical one. The procedure to achieve this conclusion is described in detail in Yu (2005), and the same assumptions are followed here.

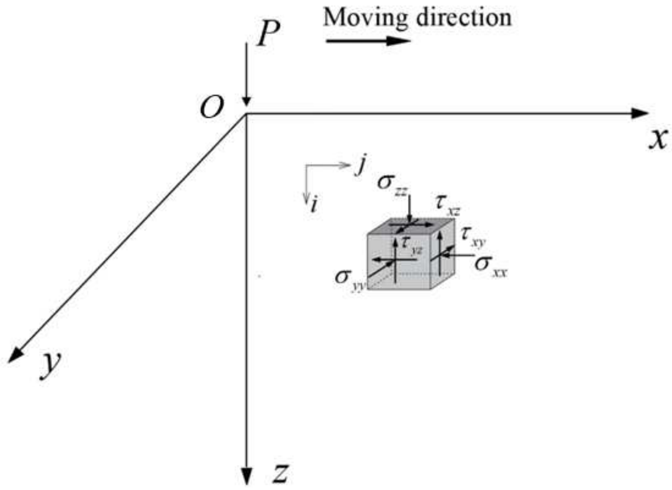

Figure 1. Half-space subject to vertically applied moving load

Consider a moving load with constant speed on the surface of a 3D half-space (Fig. 2), where *x* is the direction of load movement, *y* is perpendicular to the direction of movement, and *z* is the vertical direction. Treating tensile stresses as positive, there are six possible elastic stress (σ_e) components generated during movement: three normal stress directions: σ_{xx}^{e}, σ_{yy}^{e}, and σ_{zz}^{e}, and three shear stress directions: τ_{xy}^{e}, τ_{yz}^{e}, and τ_{xz}^{e}. Assuming the critical plane is directly below the load, the only shear stress generated in this plane is τ_{xz}^{e}, meaning τ_{xy}^{e}, τ_{yz}^{e} are zero. Furthermore, because the load is travelling in the x direction, the stresses in the y direction are always intermediate stresses, meaning this is not a critical plane either. Therefore, it is possible to consider the total elastic stress field as having just 3 stress components: σ_{xx}^{e}, σ_{zz}^{e}, and τ_{xz}^{e}.

Using a similar process of deduction for the residual stresses (σ_r), if the load did not induce τ_{xy}^{e} and τ_{yz}^{e} elastic stresses on the plane, the corresponding residual stresses will not remain after passage either. Also, the residual stress in the σ_{yy}^{r} direction will be an intermediate residual stress. To satisfy equilibrium in the vertical direction, residual stresses in the vertical σ_{zz}^{r} direction cannot occur, while the antisymmetric nature of τ_{xz}^{e} means that residual stresses cannot be induced. Therefore, the total residual stress field can be reduced to just one component: σ_{xx}^{r}.

For the geostatic stress, σ_{xx}^{0}, σ_{yy}^{0}, and σ_{zz}^{0} are principal stresses of the geostatic stress field if half-space self-weight is considered, and σ_{yy}^0 is the intermediate principal stress for any location in the plane defined by y = 0. The coefficient of earth pressure at rest $k = \mu$ / $(1-\mu)$, where μ is the Poisson's ratio; then $\sigma_{xx}^0 = k\,\sigma_{zz}^0$.

The total stress field in terms of elastic, residual and geostatic stresses can be expressed as:

$$\begin{cases} \sigma_{zz} = \lambda\sigma_{zz}^e + \sigma_{zz}^0 \\ \sigma_{xx} = \lambda\sigma_{xx}^e + \sigma_{xx}^0 + \sigma_{xx}^r \\ \tau_{xz} = \lambda\tau_{xz}^e \end{cases} \tag{2}$$

The total stress field defined by Eq. (2) must respect the yielding condition in Eq. (1). Therefore, adopting the Mohr-Coulomb criterion, defined by the cohesion and friction angle, the following inequality must be met:

$$(\sigma_1 - \sigma_3) - (\sigma_1 + \sigma_3)\sin\varphi - 2c\cos\varphi \le 0 \tag{3}$$

The principal stresses σ_1 and σ_3 are defined as:

$$\begin{cases} \sigma_1 = \dfrac{\sigma_{xx} + \sigma_{zz}}{2} + \sqrt{\left(\dfrac{\sigma_{xx} - \sigma_{zz}}{2}\right)^2 + \tau_{xz}^2} \\ \sigma_3 = \dfrac{\sigma_{xx} + \sigma_{zz}}{2} - \sqrt{\left(\dfrac{\sigma_{xx} - \sigma_{zz}}{2}\right)^2 + \tau_{xz}^2} \end{cases} \tag{4}$$

Then, substituting Eq. (4) into the Mohr-Coulomb failure criterion yields:

$$\sqrt{\left(\lambda\sigma_{xx}^e + \sigma_{xx}^0 + \sigma_{xx}^r - \lambda\sigma_{zz}^e - \sigma_{zz}^0\right)^2 + 4\left(\lambda\tau_{xz}^e\right)^2} - \left(\lambda\sigma_{xx}^e + \sigma_{xx}^0 + \sigma_{xx}^r + \lambda\sigma_{zz}^e + \sigma_{zz}^0\right)\sin\varphi - 2c\cos\varphi \le 0 \tag{5}$$

Separating the elastic and residual stress components results in a simplification:

$$f = \left(\sigma_{xx}^r + M\right)^2 + N \le 0 \tag{6}$$

where

$$\begin{cases} M = \lambda(\sigma_{xx}^r - \sigma_{zz}^e) + (\sigma_{xx}^0 - \sigma_{zz}^0) + 2\tan\varphi(c - (\lambda\sigma_{zz}^e + \sigma_{zz}^0)\tan\varphi) \\ N = 4(1 + \tan^2\varphi)[(\lambda\tau_{xz}^e)^2 - (c - (\lambda\sigma_{zz}^e + \sigma_{zz}^0)\tan\varphi)^2] \end{cases} \tag{7}$$

From above, the residual stress is unknown, making it difficult to calculate the λ value. However, if $N \leq 0$, it is possible to find one possible shakedown load factor that fulfils the condition:

$$\lambda \leq \frac{c - \sigma_{zz}^{0} \tan \varphi}{\left| \tau_{xz}^{e} \right| + \sigma_{zz}^{e} \tan \varphi} \tag{8}$$

To calculate the initial estimation of the shakedown limit load, we need to determine the minimum value of λ_{i} for a particular depth $z = i$. This involves calculating the maximum value of $|\tau_{xz}^{e}| + \sigma_{zz}^{e} \tan \varphi$ for the same depth $z = i$ due to the passage of a moving load, given that σ_{zz}^{0} is constant for the particular depth. The minimum value of λ_{i} can then be identified, resulting in λ_{i}, which serves as the initial estimation for the shakedown limit load.

However, this approach results in an "upper bound type 1" solution λ_{I}, which corresponds to the maximum limit of the lower-bound shakedown (Krabbenhøft, Lyamin, and Sloan 2007), as it disregards both yield and equilibrium constraints on residual stresses. When Eq. (1) satisfies $f = 0$, it permits the calculation of the residual stress at any point in the half-space, i.e., the smaller root $-M_{ij} - \sqrt{-N_{ij}}$ and larger root $-M_{ij} + \sqrt{-N_{ij}}$, where by the value of N_{i} should be negative. Hence, the residual stress field at a given depth $z = i$ should conform to $\max(-M_{ij} + \sqrt{-N_{ij}}) \leq \sigma_{xx}^{r} \leq \min(-M_{ij} + \sqrt{-N_{ij}})$. If the minimum larger root is less than the maximum smaller root, the half-space is in a non-shakedown state, meaning that no common residual stress satisfies $f = 0$ at any point of $z = i$. An optimization procedure is necessary to obtain a more precise approximation of the most critical shakedown load factor.

The procedure involves the following steps, as illustrated in Figure 2:

a) Compute the maximum smaller critical stress value and the minimum larger critical stress at all j locations for a given depth $z = i$, using the initial estimation of the shakedown limit load λ_{I}.

b) Determine proximity to the yield condition using either the maximum smaller critical stress or the minimum larger critical stress: If the difference between the solution and the yield condition is less than the desired threshold (e.g., 0.001), consider the shakedown limit for this depth an acceptable solution; If the solution falls outside the allowable range, employ an optimization procedure to converge the shakedown limit load to an acceptable value, for example using a bisection method.

c) Repeat the above procedure for each depth. The critical shakedown limit is the minimum value across all depths.

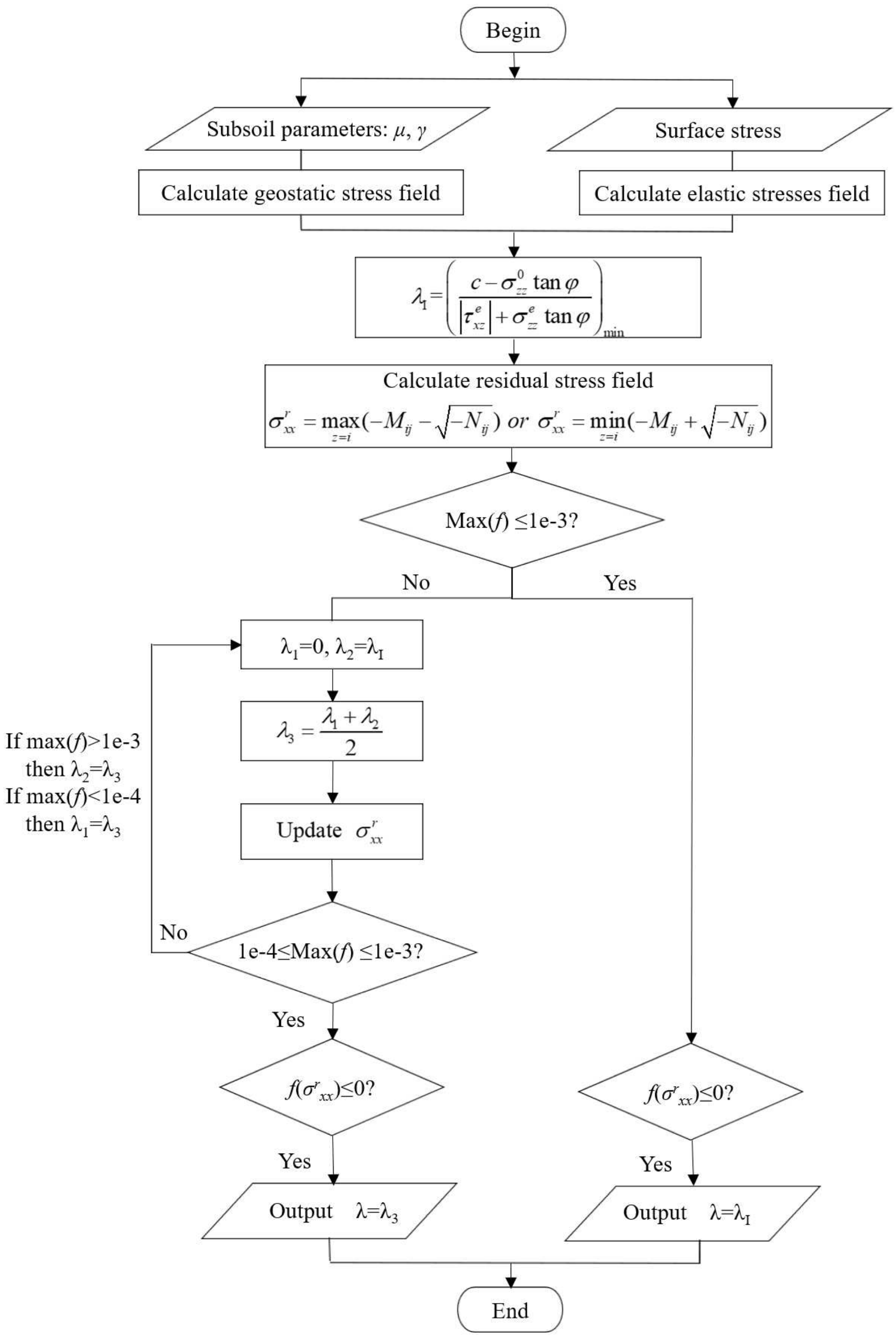

Figure 2. Flowchart of the shakedown solution

3. Model development

To obtain the stress fields needed for the start of Figure 2, shakedown limit analysis requires the domain to be invariant in the direction of the moving load. Although shakedown analysis has been attempted for ballasted tracks (Zhuang 2020; Zhuang et al. 2019; Wang and Zhuang 2021), the accuracy of shakedown limit analysis in the presence of discrete sleepers is still unclear. Similarly, slab track expansion joints introduce discontinuities in the direction of the train load, however these have until now, been disregarded in the shakedown analysis of non-ballasted track. Another requirement of shakedown analysis is that the residual stress field must remain time-independent. This is problematic for railways because the presence of track irregularities on train-track interaction causes dynamic loading that varies with position.

Considering these two challenges with applying shakedown analysis for railway slab tracks, a modelling approach was developed to overcome them. Firstly, regarding the expansion joints, a finite element method (FEM) approach was used to isolate the surface stress responses of moving train loads at representative track locations, leading to empirical approximations. These approximations, in the form of analytical equations, were then be utilized as boundary inputs into an analytical shakedown framework. Secondly, regarding the effect of dynamic train-track interaction, this is more important for differential settlement induced during track operation (Charoenwong, Connolly, Woodward, et al. 2022; Charoenwong et al. 2023; Charoenwong, Connolly, Odolinski, et al. 2022), rather than ultimate limit state design. Therefore, as proposed by Costa et al. (2018), the relevant excitation was considered to be quasi-static.

3.1 Surface stresses

A Hertzian-type load, commonly assumed for highway pavement shakedown analysis, does not accurately describe the loading exerted on a slab track system. The transfer of the axle load through the superstructure of the slab track to the trackbed modifies the load shape and magnitude on the subgrade surface, especially at the concrete base expansion joints. Below, the FEM model development and analysis is briefly outlined to investigate the diversified surface stresses on trackbed, based on which the analytical elastic stress fields can be derived.

3.1.1 Finite element track model

Due to symmetry, only half of the slab track structure is modeled. The FE mesh used for the simulation is shown in Figure 3. The track structure consists of a 176 mm high rail with a cross-sectional area of 7.745 × 105 mm^2, discretely supported on the track slab. Fasteners with a spacing of 0.63 m and a vertical stiffness of 40 kN/mm are modeled using spring elements. The track slab has a length of 5.6 m, a width of 2.5 m, and a height of 0.2 m. The self-compacting concrete has the same length and width as the track slab with a thickness of 0.1 m. Expansion joints with a width of 70 mm and 20 mm are considered for the track slab and concrete base, respectively. The track foundation consists of three layers: the upper roadbed, lower roadbed, and subgrade, each with a thickness of 0.4 m, 2.3 m, and 3.0 m, respectively. The embankment slope gradient is 1:1.5. The rail, sleepers and subgrade soil are assumed to be linear elastic materials. The material properties of the formation layers are listed in Table 1.

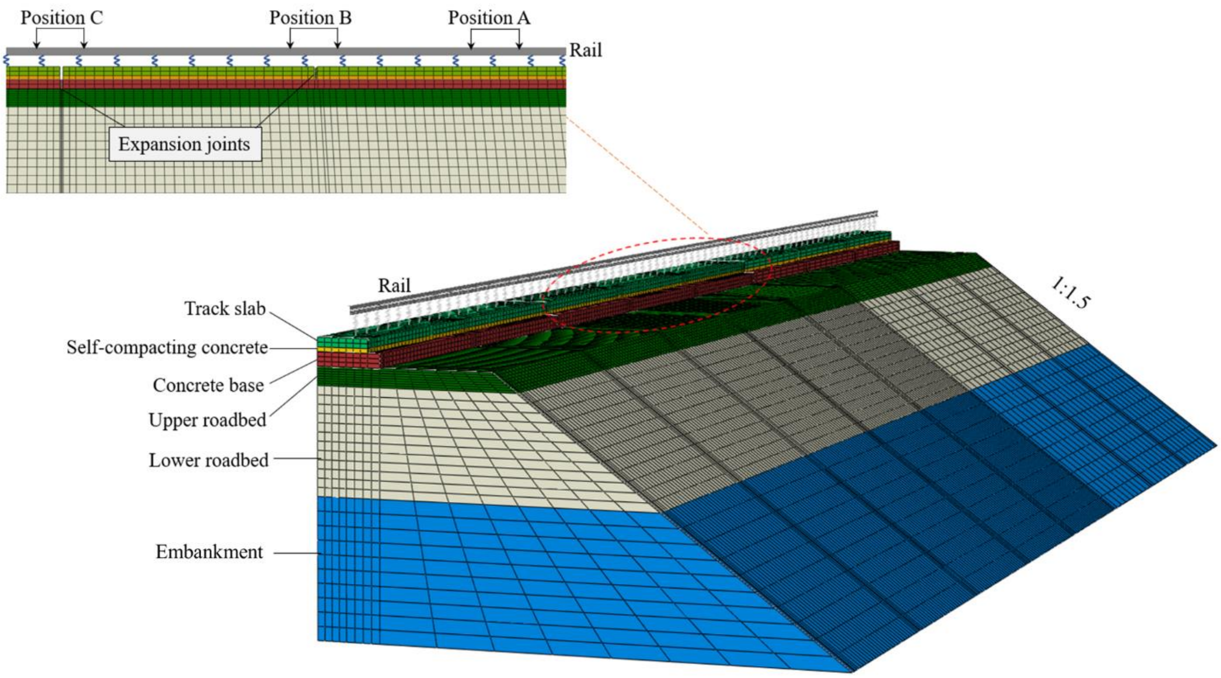

Figure 3. Finite element model of a slab track system

Table 1. Material parameters of the model components

Components	Materials	Modulus (MPa)	Poisson's ratio	Damping ratio
Rail	Steel	206,000	0.300	0.01

Track slab	C60 concrete	36,000	0.167	0.03
Self-compacting concrete	C40 concrete	32,500	0.167	0.03
Concrete base	C40 concrete	32,500	0.167	0.03
Upper roadbed	Graded gravel	228.9	0.300	0.08
Lower roadbed	Coarse fill	186.0	0.350	0.07
Subgrade	Coarse fill	163.5	0.400	0.10

The train has a design axle load of 170 kN and an axle spacing of 2.5 m, which results in each wheel load being 85 kN. The wheel/rail contact is simplified as a moving wheel load that acts on the rail. To evaluate the impact of longitudinal discontinuities, three simulation scenarios are considered, where the load is exerted at different locations on the track structures. Figure 3 shows that Position A corresponds to a force acting on the continuous structure, Position B refers to a force acting on expansion joints at the track slab level while the underlying concrete base is continuous, and Position C denotes a scenario where the load is exerted directly above expansion joints encountered in both track slab and concrete base layers.

3.1.2 Explicit expressions for two surface stresses

The stress transverse distribution of the subgrade surface at positions A, B, and C is uniform, as per the finite element model results. At positions A and B, the stress longitudinal distribution of the subgrade surface forms an approximately isosceles trapezoid, while at position C, it forms an approximately isosceles triangle. Hence, two loading modes exist for both the continuous and joint positions of the track structure, as shown in Figure 4.

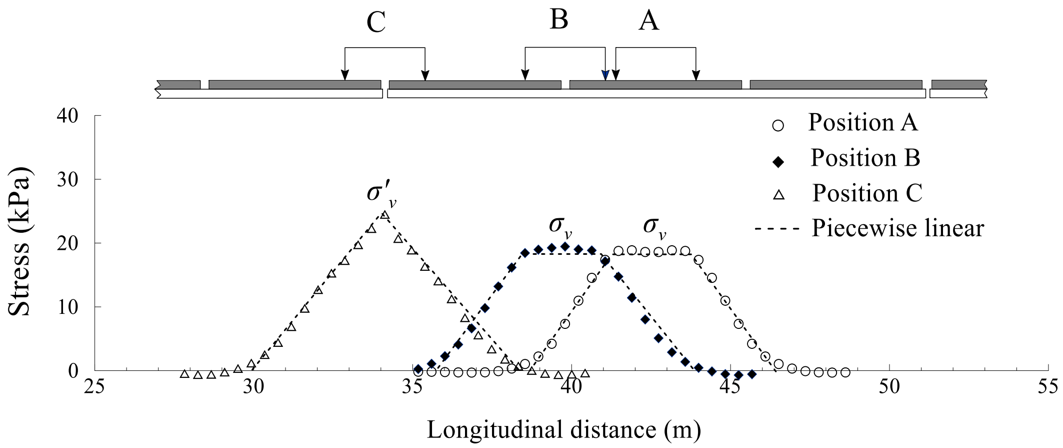

Figure 4. Three longitudinal stress distributions on the trackbed

Figure 4 displays the longitudinal stress distributions induced on the trackbed by two moving axle loads. The stress peak occurs at Position C, where expansion joints are situated on a concrete base. Stress in the transverse direction uniformly distributes at all three positions A, B, and C, with a range equivalent to the width (b) of the concrete base. At locations with continuous structures (position A) and track slab expansion joints (position B), the longitudinal stress distributions follow an isosceles trapezoid pattern. Equation (9) presents the design value of induced stress (σ_v) on the trackbed for the first pattern, considering the mechanical equilibrium conditions.

$$\sigma_v = \frac{4\varphi_k}{b(Z+L)} P_0 \tag{9}$$

where P_0 is the design axle load; L is the axle spacing; b is the width of the concrete base; Z represents the longitudinal influencing length; φ_k denotes the dynamic amplification factor which is the ratio of stress level at different speeds to that in quasi-static states (φ_k = 1.0 at 5 km/h). The prescribed structural parameters for the slab track are b=3.1 m, Z=9.0 m, and L=2.5 m.

As seen in Figure 4, when the double-axle load is located above the track joint, the trackbed load's longitudinal distribution pattern takes the form of an isosceles triangle. The finite element results indicate that, for the same design axle load, the stress magnitude ratio of a triangular load to a trapezoidal load increase with increasing speed. The value of C_v is then defined as the stress concentration coefficient of the expansion joints, which equals the stress magnitude ratio of a triangular load to a trapezoidal load. By employing the equivalence of stress and the definition of the stress concentration factor C_v, explicit expressions for the stress magnitude (σ'_v) and longitudinal influencing length (Z') are:

$$\begin{cases} Z' = \sqrt{Z^2 - L^2} \\ \sigma'_v = \dfrac{4\varphi_k}{bZ'}\dfrac{C_v}{C_0}P_0 \end{cases} \tag{10}$$

where C_0 is the stress concentration factor at 5 km/h.

Hence, for the slab track structure, train loads on the trackbed are classified into two categories: trapezoidal load on the continuous track structure and triangular load at the track joint position, as depicted in Figure 5. For two identical axle loads, the distribution length of expansion joint loading is smaller than the continuous slab loading distribution length, with a higher total load magnitude.

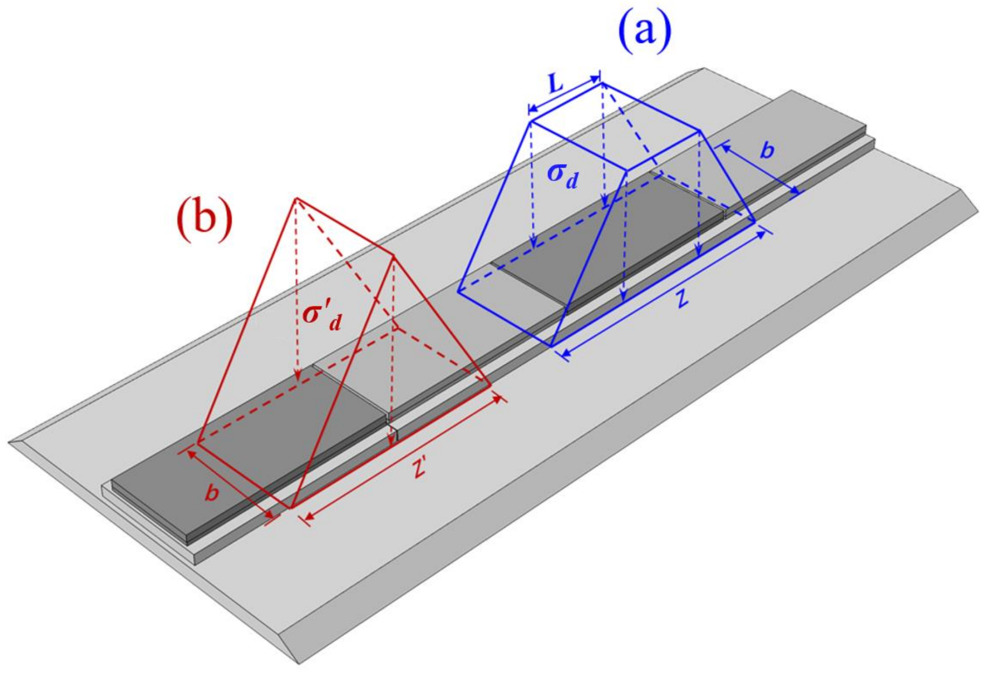

Figure 5. Simplified stress pattern on trackbed: (a) general location; (b) expansion joints (Ye et al. 2023)

3.2 Subgrade stress fields

The stress distribution on the trackbed below the concrete base is simplified by considering two loading positions of continuous slab and base expansion joints, as defined by Eqs. (9) and (10).

However, since the stress pattern changes gradually from trapezoidal to triangular as the load moves, the elastic stress field, calculated from the 3D finite element model, cannot be directly utilized for shakedown analysis. Lower-bound shakedown assumptions require a quasi-static surface load on a half-space, which leads to a time-independent residual stress field in the moving direction. By considering a single stress pattern of continuous slab loading on the subgrade surface, a shakedown limit λ_{CSL} can be determined based on the elastic stress field generated by continuous slab loading. Similarly, the shakedown limit λ_{EJL} for expansion joint loading can be derived accordingly. Since other stress magnitudes and longitudinal lengths are in an intermediate state between the two typical loading positions, the shakedown limit for the slab track structure is believed to fall within the shakedown limits due to the two stress patterns, see the induced elastic stress envelopes in Sec. 4.1. To obtain shakedown solutions for these two stress patterns, the elastic stress field can be derived from such surface stress conditions. The overall analysis procedure is provided in Figure 6.

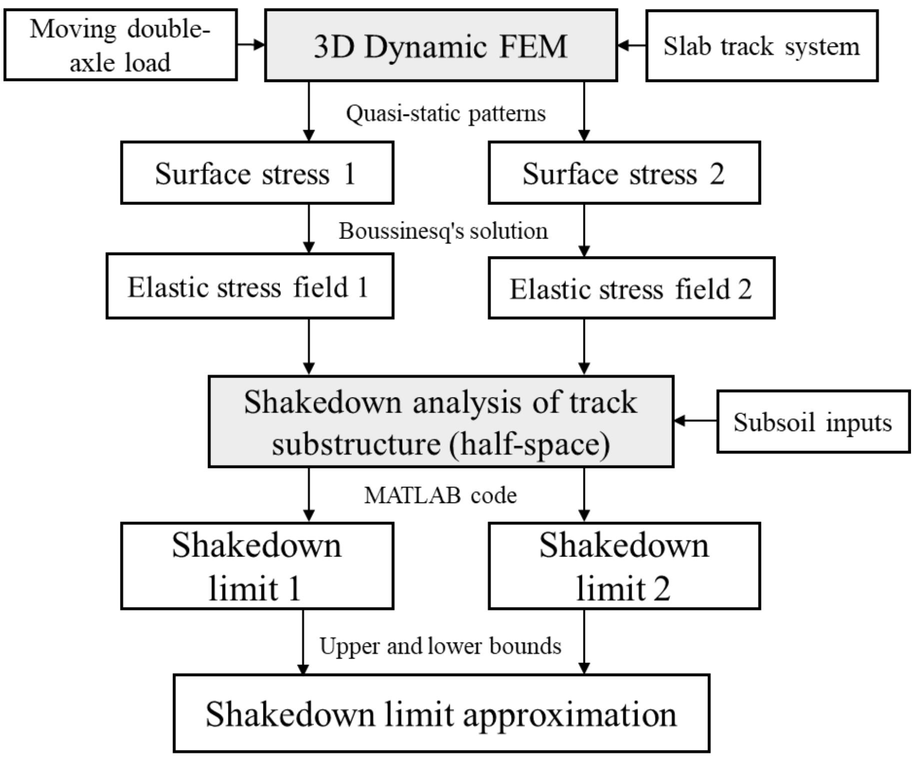

Figure 6. The overall computational logic

To obtain analytical solutions for these types of surface loads on a half- space, it is necessary to first derive the analytical solutions for uniform shaped and triangular loads (refer to Fig. 4). The derivation process is introduced below.

3.2.1 Uniform shaped fields

Boussinesq (1885) derived the stresses at any point (x, y, z) of a homogeneous, elastic, and isotropic medium subject to a concentrated load P acting on the surface of a semi-infinite half-space. This solution can be expressed by:

$$\begin{cases} (\sigma_{xx}^{e})_P = \dfrac{3P}{2\pi}\left\{\dfrac{x^2 z}{R^5} + \dfrac{1-2\mu}{3}\left[\dfrac{R^2 - z(R+z)}{R^3(R+z)} - \dfrac{x^2(2R+z)}{R^3(R+z)^2}\right]\right\} \\ (\sigma_{zz}^{e})_P = \dfrac{3P}{2\pi}\dfrac{z^3}{R^5} \\ (\tau_{xz}^{e})_P = -\dfrac{3P}{2\pi}\dfrac{xz^2}{R^5} \end{cases} \tag{11}$$

where $R^2 = x^2 + y^2 + z^2$.

A single half contact area depicted in Figure 7(a) with dimensions of A × B can be used to establish rectangular Cartesian coordinates by setting the corner of the contact area as the origin of coordinate O. Assuming a unit body with an area of dxdy, the vertical load acting on this unit body is $P_0 \cdot \mathrm{d}x \cdot \mathrm{d}y$. Consequently, the elastic stress arising from a uniform distributed vertical stress P at any depth below point O, i.e., M (0, 0, z), can be determined by (Zhuang 2020):

$$\begin{cases} (\sigma_{xx}^{e})_P = \dfrac{P}{2\pi}\left\{\operatorname{atan}\dfrac{AB}{z\sqrt{A^2+B^2+z^2}} - \dfrac{ABz}{(A^2+z^2)\sqrt{A^2+B^2+z^2}}\right. \\ \qquad\qquad \left. +(1-2\mu)\left[\operatorname{atan}\left(\dfrac{B}{A}\right) - \operatorname{atan}\left(\dfrac{Bz}{A\sqrt{A^2+B^2+z^2}}\right) - \operatorname{atan}\left(\dfrac{AB}{z\sqrt{A^2+B^2+z^2}}\right)\right]\right\} \\ (\sigma_{zz}^{e})_P = \dfrac{P}{2\pi}\left[\dfrac{ABz(A^2+B^2+2z^2)}{(A^2+z^2)(B^2+z^2)\sqrt{A^2+B^2+z^2}} + \operatorname{atan}\dfrac{AB}{z\sqrt{A^2+B^2+z^2}}\right] \\ (\tau_{xz}^{e})_P = -\dfrac{P}{2\pi}\left[\dfrac{B}{\sqrt{B^2+z^2}} - \dfrac{Bz^2}{(A^2+z^2)\sqrt{A^2+B^2+z^2}}\right] \end{cases} \tag{12}$$

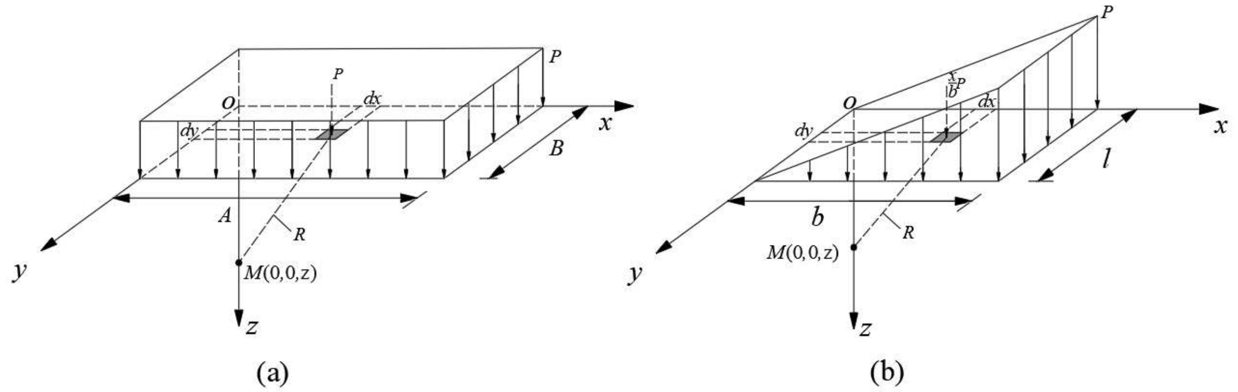

Figure 7. Schematic of elastic stress in half-space: (a) uniform shaped loading, (b) triangular loading

By employing the principle of superposition, the elastic stress field induced by the uniform load P_0 at any point (x, y, z) can be obtain as follows:

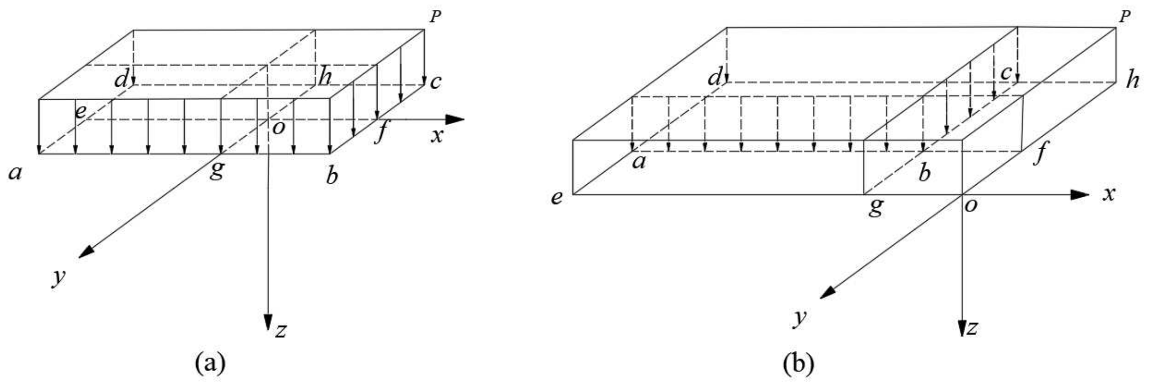

Figure 8. The elastic stress field calculated by the corner point method: (a) point *O* beneath the rectangular area; (b) point *O* outside the rectangular area

When z > 0 beneath the surface, a uniform load acts on a rectangular contact area underside *abcd*, as illustrated in Figure 8(a). To determine the elastic stress increment at any depth below point *O*, two sublines *ef* and *gh* can be drawn parallel to the longer and shorter sides of the rectangular contact area, respectively. Point *O* serves as the common corner of four rectangles 1, 2, 3, and 4. Thus, the elastic stress increment at any depth beneath *O* is the aggregate of elastic stress increments of the aforementioned four new rectangular contact areas.

$$(\sigma_{ij}^{e})_{abcd} = (\sigma_{ij}^{e})_{oeag} + (\sigma_{ij}^{e})_{ogbf} + (\sigma_{ij}^{e})_{ofch} + (\sigma_{ij}^{e})_{ohde} \tag{13}$$

In the event that point O lies beyond the range of the rectangular contact area underside, the current rectangular contact area underside should first be expanded to place point O beneath the corner of an assumed contact area underside, as illustrated by the dotted line in Figure 8(b). Consequently, the elastic stress increment at any arbitrary depth below point O is the total of the elastic stress increments at O caused by the four respective rectangular contact area undersides (*ohed*, *Ohcg*, *Ofae*, and *Ofbh*).

$$(\sigma_{ij}^{e})_{abcd} = (\sigma_{ij}^{e})_{ohed} - (\sigma_{ij}^{e})_{ohcg} - (\sigma_{ij}^{e})_{ofae} + (\sigma_{ij}^{e})_{ofbh} \tag{14}$$

3.2.2 Triangular shaped fields

Similar to the rectangular uniform load formula, for the triangular load acting on the rectangular area in Figure 7(b), with a length of b and a width of l, setting the origin coordinate O to be the zero-load corner of the contact area. Taking a unit integral body with the area of dxdy, the vertical load on the integral area is $\frac{x}{b}P\mathrm{d}x\mathrm{d}y$. By integrating across the load area yields, the analytical elastic stress to the triangular load P at any arbitrary point M (0, 0, z) below point O can be obtained:

$$(\sigma_{xx}^{e})_P = \frac{3P}{2\pi}\left\{\frac{z}{b}\int_0^b\int_0^l \frac{x^3}{R^5}dxdy + \frac{1-2\mu}{3b}\left[\int_0^b\int_0^l \frac{xdxdy}{R(R+z)} - z\int_0^b\int_0^l \frac{xdxdy}{R^3} - \int_0^b\int_0^l \frac{(2R+z)x^3dxdy}{R^3(R+z)^2}\right]\right\} \tag{15}$$

The corresponding sub-item in Eq. (15) can be calculated as followings:

$$\int_0^b\int_0^l \frac{x^3}{R^5}dxdy = -\frac{2}{3}\left[\ln\frac{z(l+\sqrt{a^2+b^2+z^2})}{\sqrt{z^2+b^2}(l+\sqrt{l^2+z^2})} + \frac{b^2 l}{2\left(b^2+z^2\right)\sqrt{a^2+b^2+z^2}}\right] \tag{16}$$

$$\begin{aligned}\int_0^b\int_0^l \frac{x}{R(R+z)}dxdy = b&\left(\operatorname{atan}\frac{l}{b} - \operatorname{atan}\frac{lz}{b\sqrt{b^2+l^2+z^2}}\right)\\ &+ z\ln\frac{z(l+\sqrt{b^2+l^2+z^2})}{\sqrt{b^2+z^2}(l+\sqrt{l^2+z^2})} - l\ln\left(\frac{z+\sqrt{l^2+z^2}}{z+\sqrt{b^2+l^2+z^2}}\right)\end{aligned} \tag{17}$$

$$\int_0^b\int_0^l \frac{x}{R^3}dxdy = -\ln\frac{z(l+\sqrt{a^2+b^2+z^2})}{\sqrt{z^2+b^2}(l+\sqrt{l^2+z^2})} \tag{18}$$

$$\int_0^b\int_0^l \frac{(2R+z)x^3dxdy}{R^3(R+z)^2} = b\left(\operatorname{atan}\frac{l}{b} - \operatorname{atan}\frac{lz}{b\sqrt{b^2+l^2+z^2}}\right) + 2z\ln\frac{z(l+\sqrt{b^2+l^2+z^2})}{\sqrt{b^2+z^2}(l+\sqrt{l^2+z^2})} - 2l\ln\left(\frac{z+\sqrt{l^2+z^2}}{z+\sqrt{b^2+l^2+z^2}}\right) \tag{19}$$

Substituting Eqs. (16) to (19) into Eq. (15), the analytical solution $(\sigma_{xx}^e)_{P_0}$ for can be given by:

$$(\sigma_{xx}^e)_P = \frac{-Pz}{\pi b}\left[\ln\frac{z(l+\sqrt{b^2+l^2+z^2})}{\sqrt{b^2+z^2}(l+\sqrt{l^2+z^2})} + \frac{lb^2}{2(b^2+z^2)\sqrt{b^2+l^2+z^2}}\right] + \frac{P(1-2\mu)l}{2\pi b}\ln\left(\frac{z+\sqrt{l^2+z^2}}{z+\sqrt{b^2+l^2+z^2}}\right) \tag{20}$$

Likewise, the elastic stress $(\sigma_{zz}^e)_P$ and $(\sigma_{xz}^e)_P$ required for shakedown analysis can be obtained as:

$$(\sigma_{zz}^e)_P = \frac{3P}{2\pi}\int_0^b\int_0^l \frac{xz^3}{bR^5}dxdy = \frac{Pzl}{2\pi b}\left[\frac{l}{\sqrt{l^2+z^2}} - \frac{z^2}{(b^2+z^2)\sqrt{b^2+l^2+z^2}}\right] \tag{21}$$

$$(\sigma_{xz}^e)_P = \frac{-3P}{2\pi}\int_0^b\int_0^l \frac{x^2z^2}{bR^5}dxdy = \frac{Pz^2}{2\pi(b^2+z^2)}\left[\frac{l}{\sqrt{b^2+l^2+z^2}} - \frac{(b^2+z^2)}{bz}\operatorname{atan}\frac{bl}{z\sqrt{b^2+l^2+z^2}}\right] \tag{22}$$

Seen in Figure 9, by using the principle of superposition, the elastic stress field induced by the triangular load *OAB* at any point *M* (x, 0, z) in the *xoz* plane can be expressed by:

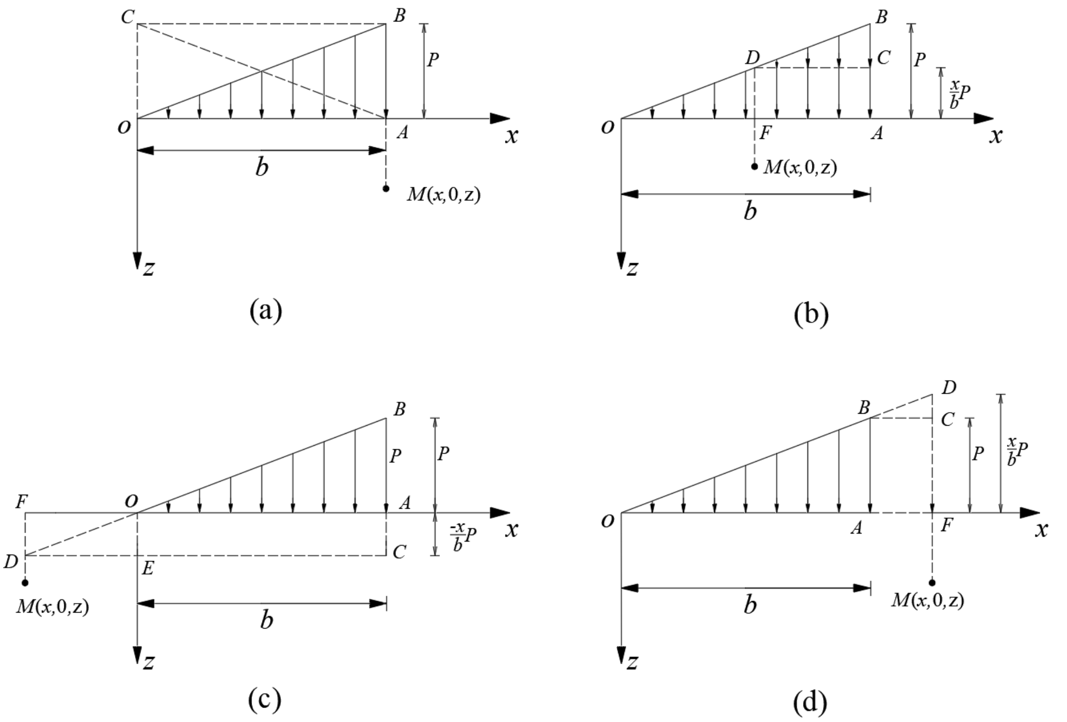

Figure 9. Four scenarios of the corner point method to calculate elastic stress field

a) When point M is located below the point of A, which is P load corner of the triangular load OAB, the elastic stress field $(\sigma_{ij}^{e})_{P}$ at point M is the difference between the elastic stress field generated by the rectangular load $OABC$ and the triangular load OAC:

$$(\sigma_{ij}^{e})_{OAB} = (\sigma_{ij}^{e})_{OABC} - (\sigma_{ij}^{e})_{OAC} \tag{23}$$

b) When point M is located below point F on line segment OA, the triangle load OAB is split into three sub-loads: triangular loads OFD and DCB, and rectangular load $FADC$. In this case, the elastic stress field $(\sigma_{ij}^{e})_{P}$ generated by the triangular load OAB at point M is the sum of the three sub-loads:

$$(\sigma_{ij}^{e})_{OAB} = (\sigma_{ij}^{e})_{OFD} + (\sigma_{ij}^{e})_{FACD} + (\sigma_{ij}^{e})_{CBD} \tag{24}$$

c) When point M is located below point F outside the line segment AO, as shown in Figure 9(c), the elastic stress field $(\sigma_{ij}^{e})_{P}$ generated by the triangular load OAB at point M is determined by Eq. (25):

$$(\sigma_{ij}^e)_{OAB} = (\sigma_{ij}^e)_{CBD} - (\sigma_{ij}^e)_{AFDC} + (\sigma_{ij}^e)_{OFD} \tag{25}$$

d) When point *M* is located below point *F* outside the line segment *OA*, as shown in Figure 9(d), the elastic stress field $(\sigma_{ij}^e)_P$ is derived from Eq. (26):

$$(\sigma_{ij}^e)_{OAB} = (\sigma_{ij}^e)_{OFD} - (\sigma_{ij}^e)_{AFCB} + (\sigma_{ij}^e)_{CDB} \tag{26}$$

3.2.3 Elastic stress solution for continuous slab loading and expansion joint loading

By combining uniform and triangular shaped fields, elastic stress solutions for continuous slab loading and expansion joint loads on the surface of a half-space can be obtained. The continuous slab loading can be decomposed into a uniform rectangular load and two triangular loads, while the expansion joint loading can be separated into two sub-triangular loads. Figure 10 displays the shakedown limits for the two stress patterns with and without geostatic stresses, considering parameters μ = 0.3, c = 1 kPa.

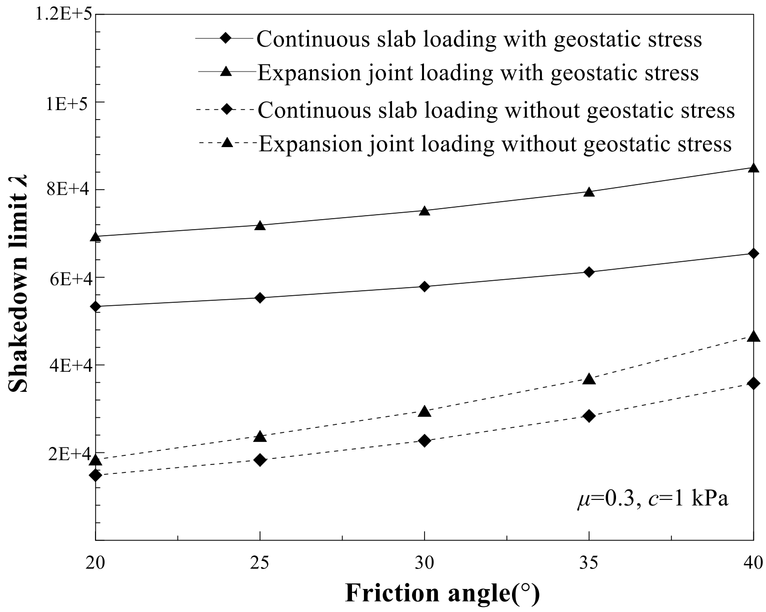

Figure 10. Shakedown limits for continuous slab loading and expansion joint loading with and without geostatic stress fields

Figure 10 demonstrates that the inclusion of geostatic stress can significantly raise the shakedown limit. The shakedown limits for expansion joint loading, with and without geostatic stress state, are higher than the corresponding values for continuous slab loading. This indicates that triangular loads at expansion joints are a more conservative mode of force compared to trapezoidal loads at general positions for the same magnitude. Furthermore, the discrepancy in shakedown between the two stress patterns intensifies with the friction angle of subsoil.

4. Validation

4.1 Elastic stress envelopes

Figure 11 shows the stress envelopes at three typical depths of: 0 m, 0.4 m, and 2.7 m, within the subgrade.

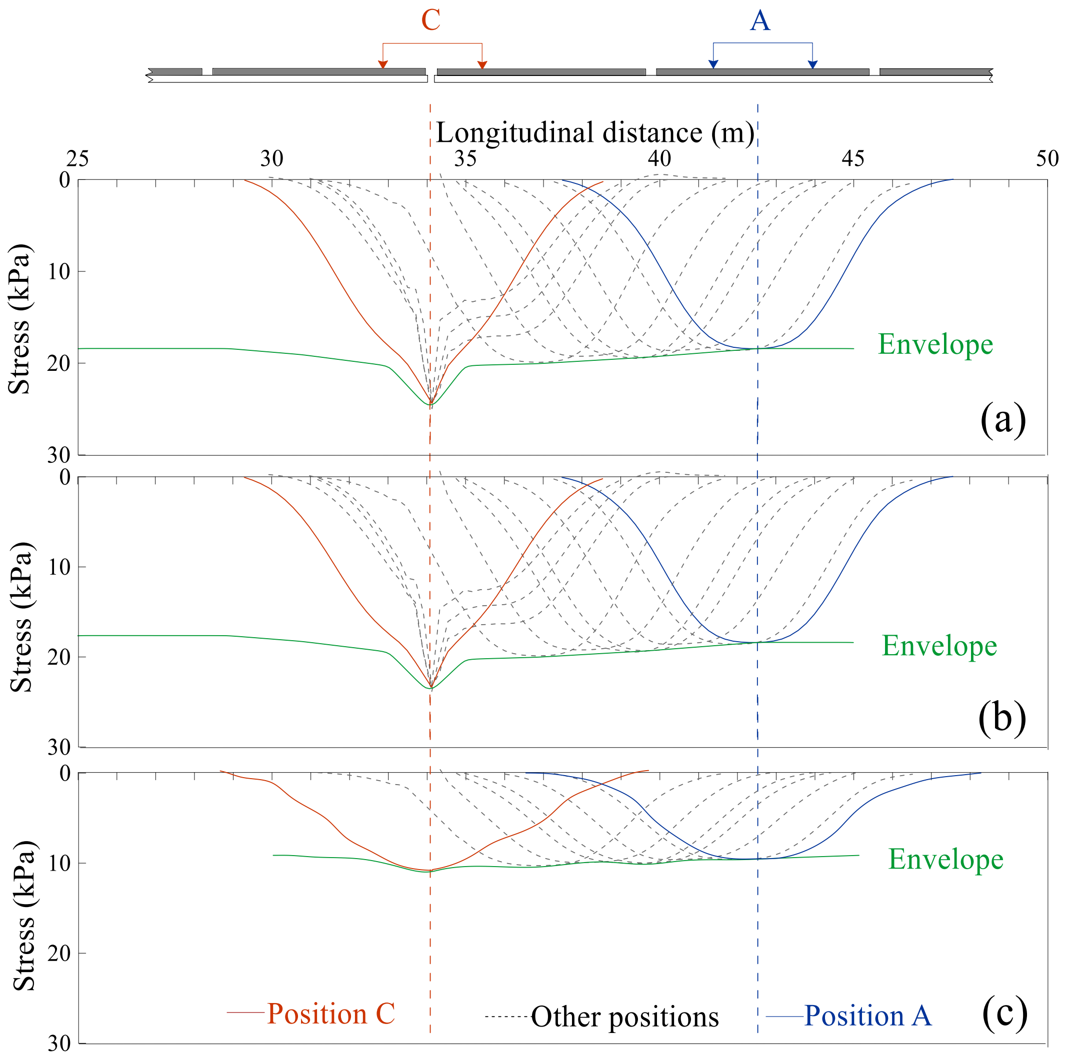

Figure 11. Stress envelopes at different subgrade depths: (a) 0 m (surface); (b) 0.4 m; (c) 2.7 m

In the analysis of shakedown for slab track substructures, the elastic stress fields are only affected by the stress patterns on the subgrade surface. When subjected to the same axle load, the continuous slab loading located at track structure midpoints result in the minimum stress magnitude, whereas the expansion joint loading leads to the largest stress magnitude. Stress magnitudes at other positions are between these two extremes, indicating that the resulting elastic stress fields also fall in between. As illustrated in Figure 11, the stress magnitude envelope at depths of 0.4 m and 2.7 conform to the same law observed on the surface, implying that the elastic stress fields always lie within the bounds of those generated by continuous slab loading and expansion joint loading.

4.2 Stress attenuation along the depth

The stress patterns on the roadbed surface have been identified as being trapezoidal and triangular in shape. Boussinesq's equations can be used to determine the variation of stress with depth. Figure 14(a) illustrates a comparison between analytical solutions and numerical simulations of stress attenuation in the track foundation, with P_0=170 kN and v=5 km/h. The attenuation coefficients are obtained by normalizing the stress values with respect to the baseline on the roadbed. Figure 14(b) shows a comparison of stress attenuation coefficients with increasing depth.

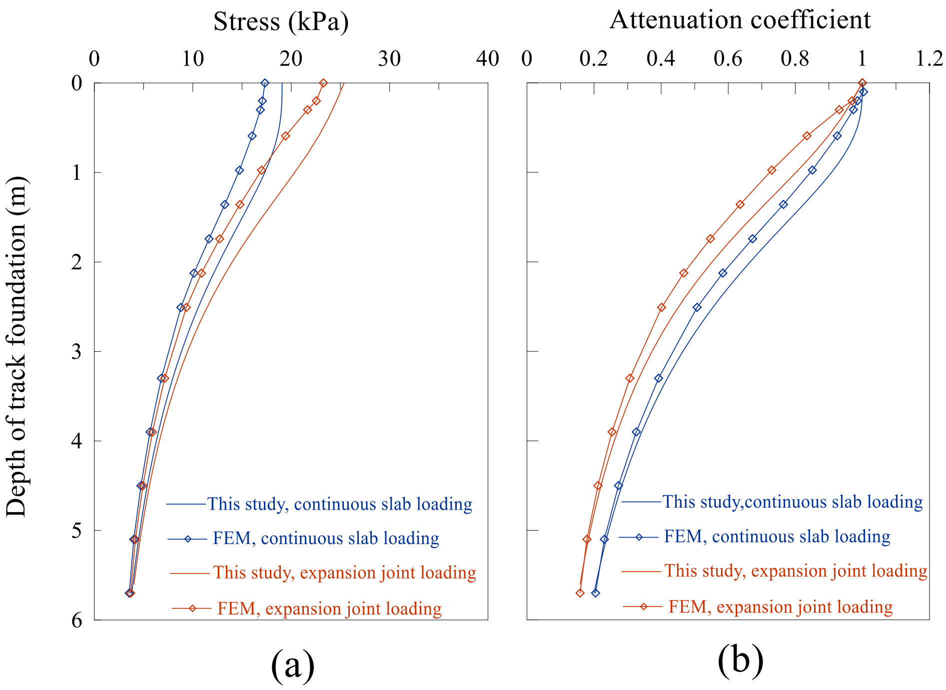

Figure 12. Stress attenuation in slab track foundation: (a) stress variation in depth from surface level; (b) normalised stress attenuation

The numerical simulations show smaller stress values than the analytical solution at the same depth. When the operating speed is 5 km/h, stress differences of 1.75 kPa and 2.10 kPa for continuous and discontinuous structures are observed using both methods on the roadbed. At the base of the upper roadbed (0.4 m), these differences increase to 2.32 kPa and 2.90 kPa, before decreasing to 1.57 kPa and 1.84 kPa at the base of the lower roadbed (2.7 m). The maximum difference in stress values between the two methods throughout the depth of interest is 2.32 kPa and 2.90 kPa, which is considered acceptable. The maximum difference in attenuation coefficient obtained by the two methods is 4.2%, suggesting that the derived stress patterns are of sufficient accuracy and lead to a conservative track foundation design.

4.3 Shakedown limits compared with existing studies

The shakedown limit of continuous slab loading on a homogenous half-space was validated by comparing the calculation results against those computed using a simplified track analysis (Wang, Liu, and Yang 2018). In the analysis, the superstructure components were considered to act together as a single infinite Euler-Bernoulli beam, while the supporting substructure was simplified as a Winkler's foundation. The relation between the reaction modulus k and the elastic modulus E of the soil was proposed (Liu et al. 2018):

$$k = \frac{0.583 E_b I}{b^{1.267} d^{3.733}} \tag{27}$$

with

$$d = \left(\frac{(1-\mu^2) E_b I}{E} \right)^{1/3} \tag{28}$$

where μ is Poisson's ratio of the soil; b is the half width of the slab track; $E_b I$ can be calculated from the material properties in Table 2.

Table 2. Material properties and dimensions of the key components of track superstructure

Track Components	Modulus (MPa)	Width (m)	Height (m)	Second moment of area I (m^4)
Rail	206,000	0.15	0.172	3.06×10^{-5}
Track slab	36,000	0.167	0.2	1.67×10^{-3}

Self-compacting concrete	32,500	0.167	0.1	2.08×10^{-4}
Concrete base	32,500	0.167	0.3	6.98×10^{-3}

Then, a single-axle load P_0 can be converted into a distributed load p on the top of the substructure using:

$$p = p_0 e^{-\eta|x|}(\cos\eta(x) + \sin\eta|x|) \quad (29)$$

where $p_0=P_0\,\eta/2b$; $\eta=(kb/4E_bI)^{0.25}$.

Figure 13(a) exhibits the pressure distribution for a dual-axle load employing Eq. (29) and the continuous slab loading on the trackbed surface. The pressure is assumed to be distributed uniformly over the width of the concrete base in the transverse direction. Figure 13(b) displays the difference in shakedown limit between the two stress patterns, with different friction angles. The shakedown limits obtained through simplified track analysis are slightly lower than those of the proposed continuous slab loading. However, the difference is less than 5%, indicating the accuracy of the continuous slab loading at general positions.

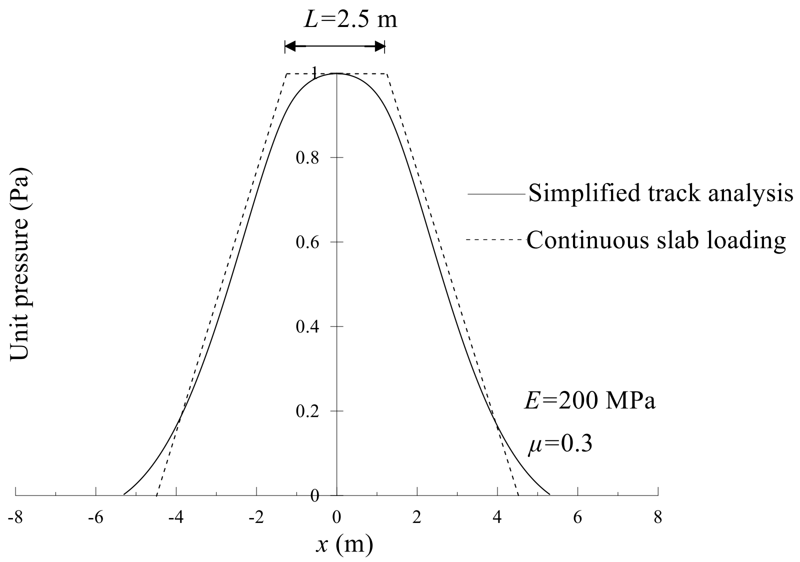

(a)

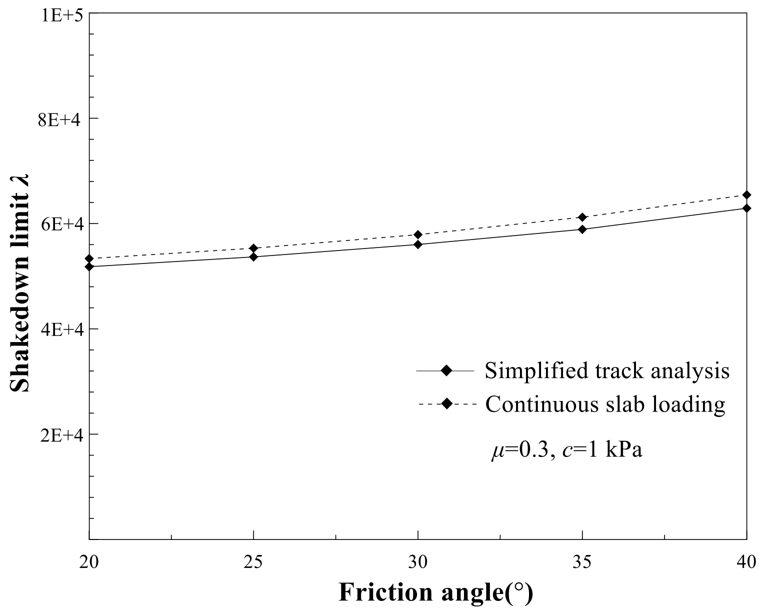

(b)

Figure 13. Comparison of simplified track analysis and the proposed model: (a) longitudinal distribution of surface stresses; (b) shakedown limits versus soil friction angles considering geostatic stress

5. Analysis

Simulations are conducted on a homogeneous half-space with friction angles φ of 20°, 25°, 30°, 35°, and 40°, cohesions c of 1 kPa, 2 kPa, and 5 kPa, Poisson's ratios μ of 0.3, 0.35, 0.4, and 0.5, and bulk density of 2 000 kg/m^3. It should be noted that the cohesion in a compacted coarse fill for a track foundation is a result of grain interlocking, dilatancy, and rearrangement of grains. The elastic stresses are calculated using the equations described in Section 4.1 for both continuous slab and expansion joint loading. The shakedown limit is normalized with respect to the load as $\lambda_{\text{normalised}} = \lambda P_0/c$ since it is always proportional to the value of cohesion (Wang, Liu, and Yang 2018). The evolution of the normalized shakedown limit is compared while considering or neglecting the geostatic stress state.

5.1 Friction angle

Figure 14 and Figure 15 illustrate the impact of φ on the normalized shakedown limit, which varies with Poisson's ratio μ. As anticipated, increasing the friction angle results in a higher shakedown limit for continuous slab loading and expansion joint loading alike. In the case of μ=0.3

neglecting the geostatic stress state, the normalized shakedown limits increase by approximately 141% for continuous slab loading with friction angle increasing from 20° to 40°. Although the Poisson's ratio is expressed as a function of elastic stress in Eq. (12) and Eq. (20), it rarely affects the normalized shakedown limit load, with the curves converging for μ = 0.3 0.35, 0.4 and 0.5 for both continuous slab loading and expansion joint loading. However, when considering geostatic effects, the overall effect of friction angle on the normalized shakedown limit remains similar, while the Poisson's ratio has a significant impact on the shakedown limit. For instance, when φ = 20°, the normalized shakedown limit increases by 186% and 187%, respectively, for continuous slab loading and expansion joint loading as the Poisson's ratio increases from 0.3 to 0.5. Detailed data for generating Figure 14 and Figure 15 is provided in Appendix A.

Furthermore, if the geostatic stress state is ignored, the critical depth decreases as the friction angle increases, indicating that the structure failure occurs closer to the surface. However, when the at rest state is taken into account, the critical depths are always 0 m for μ = 0.3 and 0.35, which implies that the failure occurs at the surface. For instance, in the case of μ = 0.3, Figure 16 illustrates the typical critical residual stress fields of the continuous slab loading for both φ = 20° and φ = 40° conditions. The critical depths are both null for φ = 20° and φ = 40° when considering geostatic stress, while without the geostatic stress the critical depth decreases from 1.37 m to 1.05 m.

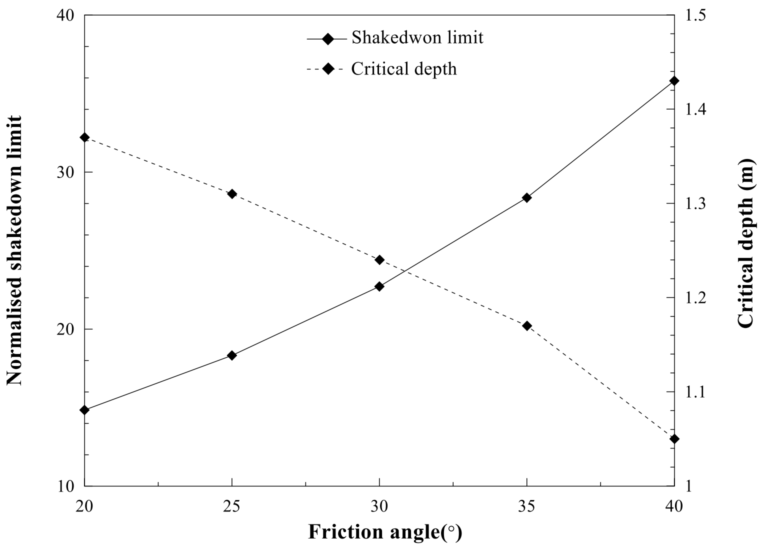

(a)

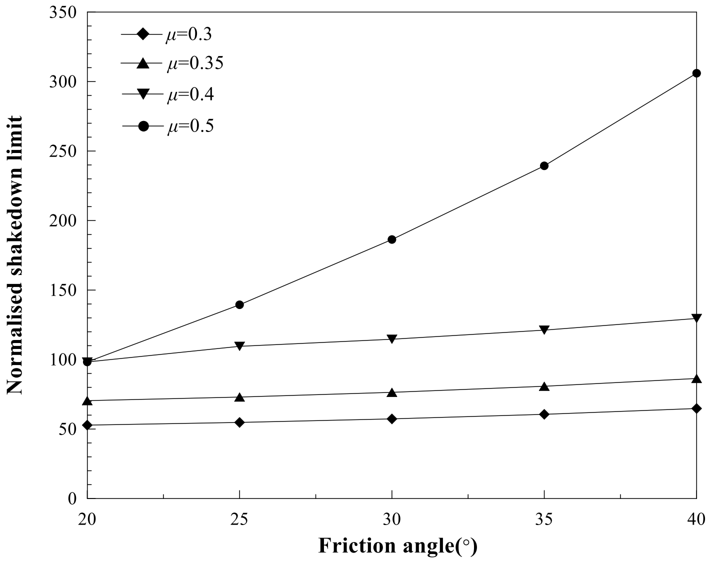

(b)

Figure 14. Normalised shakedown limit with continuous slab loading: (a) without geostatic stress; (b) with geostatic stress

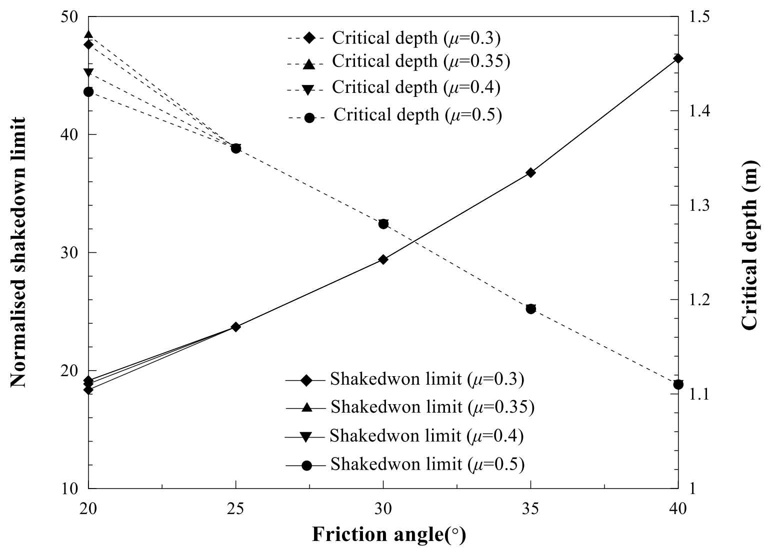

(a)

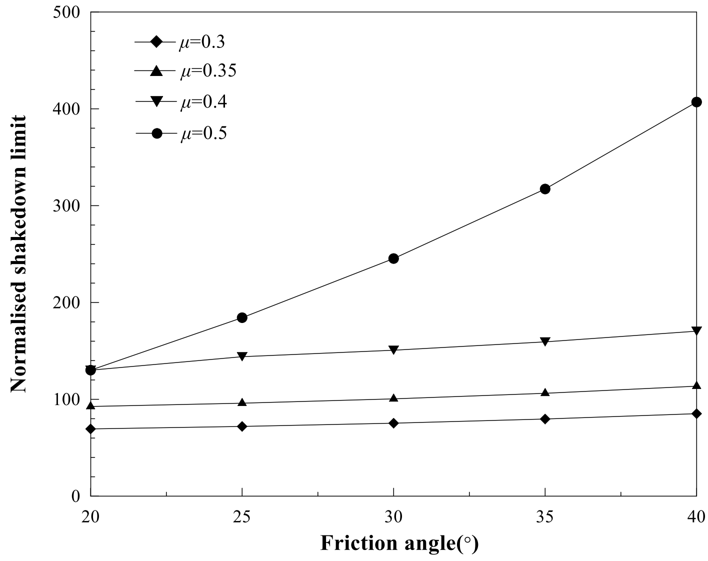

(b)

Figure 15. Normalised shakedown limit for expansion joint loading: (a) without geostatic stress; (b) with geostatic stress

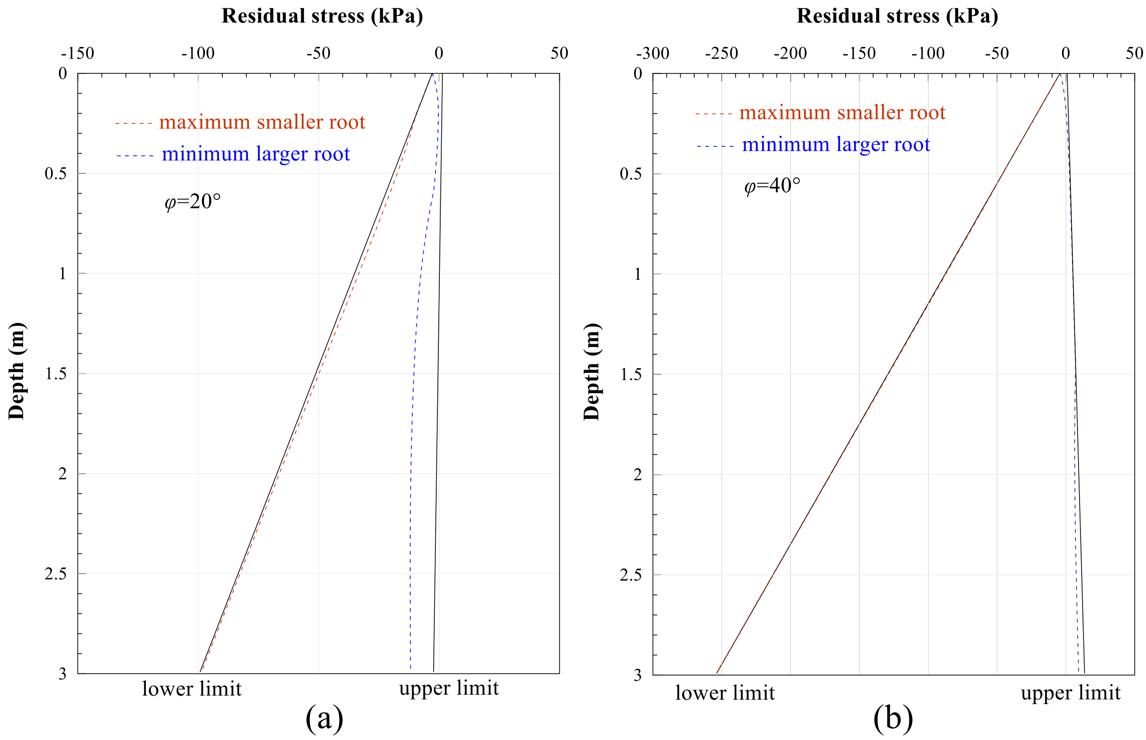

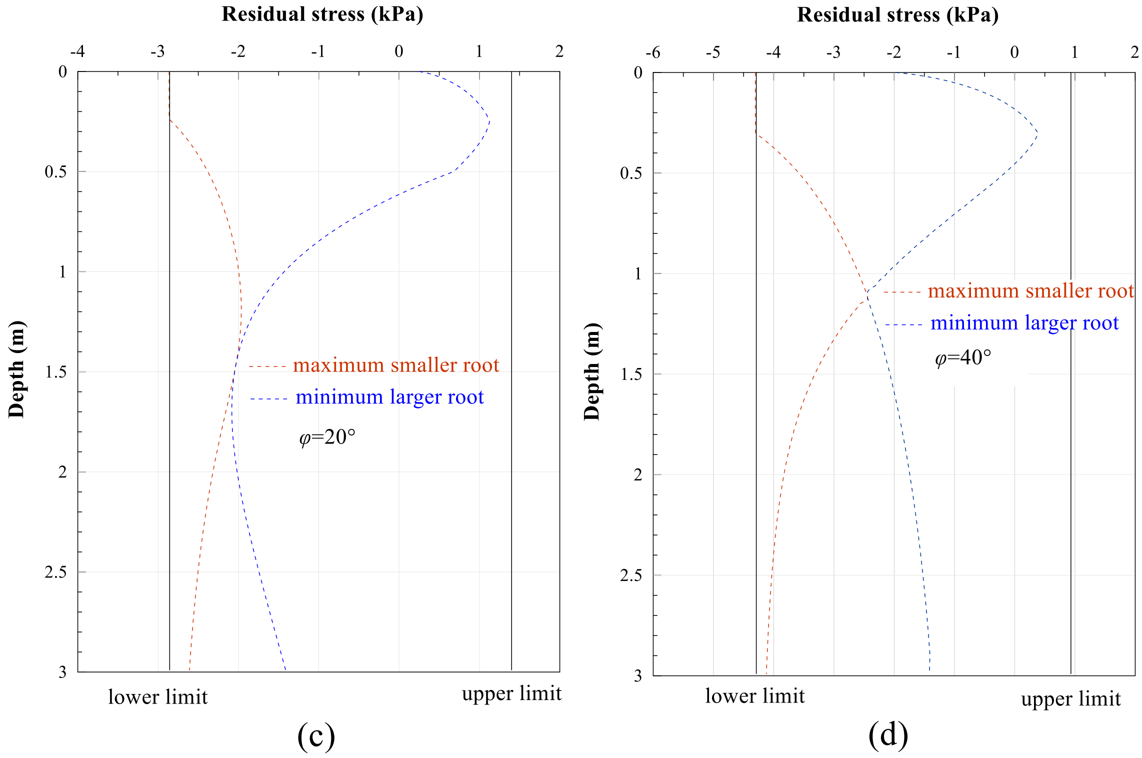

Figure 16. Distributions of critical residual stresses of continuous slab loading: (a) $\varphi = 20°$ with geostatic stress; (b) $\varphi = 40°$ with geostatic stress; (c) $\varphi = 20°$ without geostatic stress; (d) $\varphi = 40°$ without geostatic stress

5.2 Cohesion

Taking Poisson's ratio $\mu = 0.3$ as a base model, Figure 17 and Figure 18 illustrate the impact of different cohesions on the normalized shakedown limit with varying friction angle φ for continuous slab loading and expansion joint loading. Since the shakedown limit λP_0 is always proportional to the value of cohesion when ignoring geostatic stresses, cohesion has no effect on the normalized shakedown limit for all cases shown in Figure 17(a) and Figure 18(a). However, when considering the geostatic stresses, λP_0 is not always proportional to cohesion, as demonstrated by Eq. (8), which shows that the shakedown initial value changes from c to $c - \sigma_{zz}^0 \tan\varphi$. The normalized shakedown limit decreases at cohesive values of 5 kPa and 10 kPa (φ increasing from 20° to 40°) for continuous slab loading, relative to the values of c = 1 kPa and 2 kPa, as depicted in Figure 17(b). Similarly, for expansion joint loading, the normalized shakedown limit decreases at cohesive values of 5 kPa and 10 kPa (φ increasing from 20° to 30°) compared to the corresponding values of c = 1 kPa and 2 kPa, as illustrated in Figure 18(b).

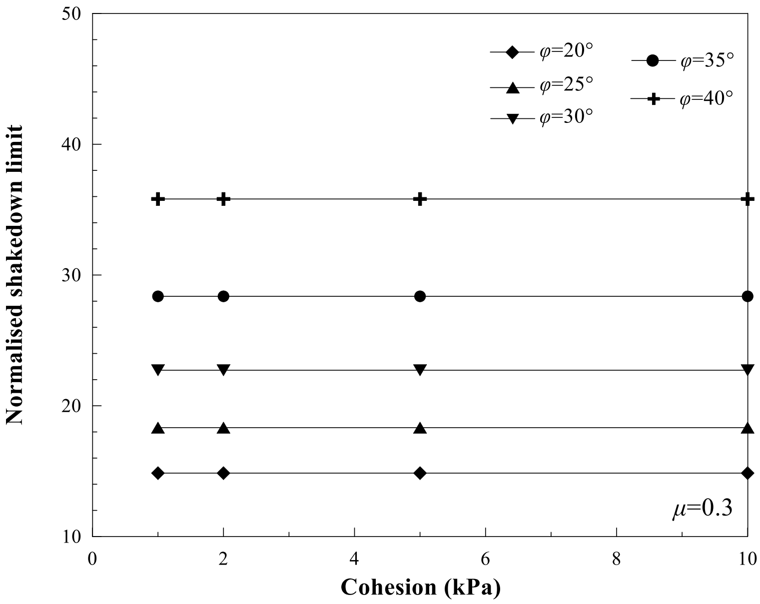

(a)

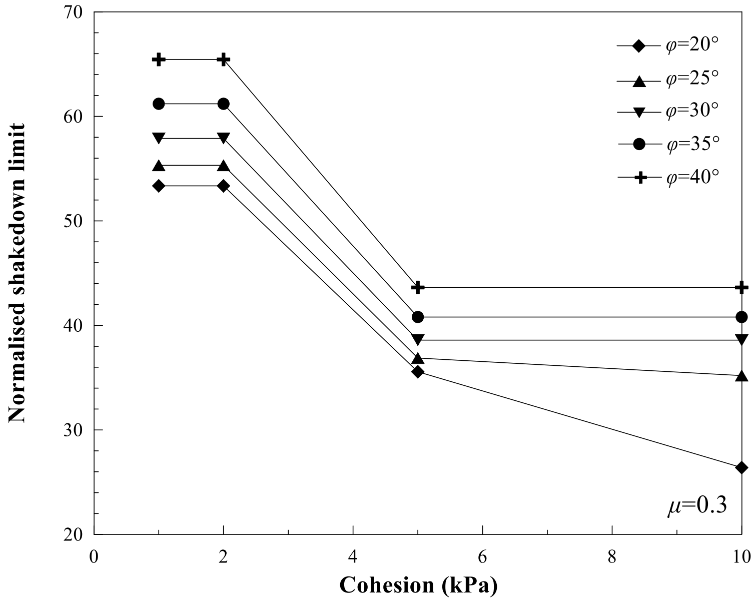

(b)

Figure 17. Normalised shakedown limit for continuous slab loading versus soil cohesion: (a) without geostatic stress; (b) with geostatic stress

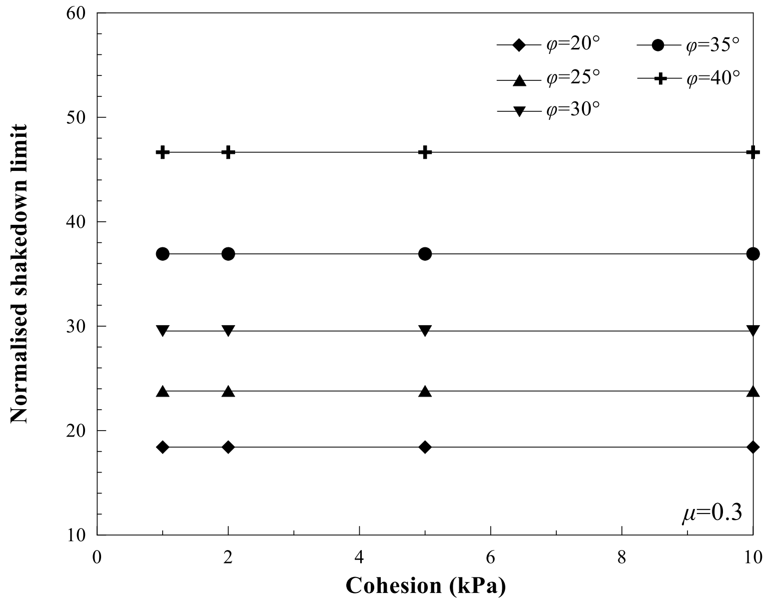

(a)

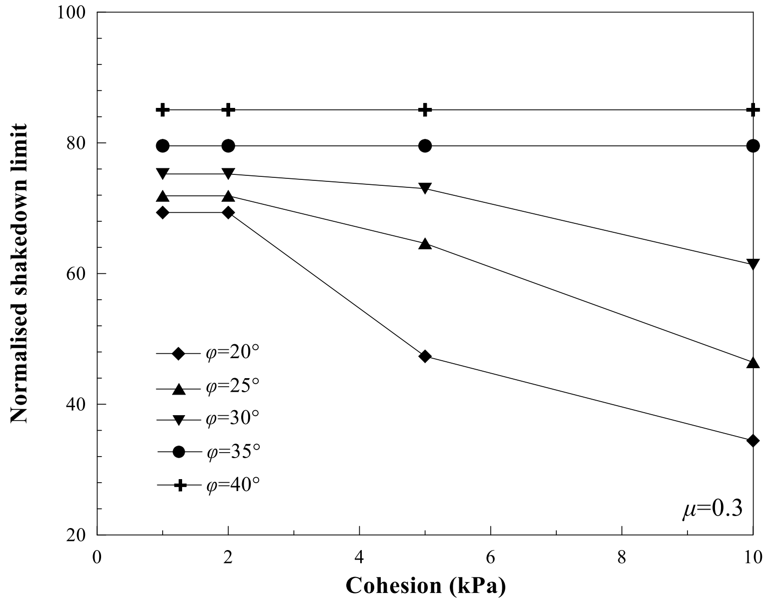

(b)

Figure 18. Normalised shakedown limit of expansion joint loading for varying cohesions: (a) without geostatic stress; (b) with geostatic stress

5.3 Poisson's ratio

Figure 19 and Figure 20 depict the effect of Poisson's ratio μ on the normalized shakedown limit, which changes with friction angle φ. Four Poisson's ratios of 0.3, 0.35, 0.4, and 0.5 were considered, where μ=0.3 is a common Poisson's ratio for subsoil and μ=0.5 means the substructure is in isotropic consolidation. As mentioned in Section 5.1, Poisson's ratio rarely impacts the normalized shakedown limit for continuous slab loading and expansion joint loading when disregarding the geostatic stress state. However, accounting for the geostatic stress state, a greater Poisson's ratio results in a higher shakedown limit. Poisson's ratio μ affects the geostatic stress state via the coefficient of earth pressure, $k = \mu / (1-\mu)$, which is an increasing function of μ. Thus, considering the geostatic stresses, increasing μ elevates the stress component, $\sigma_{xx}^0 = k\,\sigma_{zz}^0$, which makes the difference between vertical stress σ_{zz}^0 and horizontal stress σ_{xx}^0 smaller. In particular, the first principal stress is equal to the third principal stress with Poisson's ratio increasing to 0.5. The Mohr circle of subsoil with geostatic stress changes to a point in the Mohr circle coordinate system, which means no shear stress occurs in y=0 plane (see Figure 1). Therefore, larger Poisson ratios can provide a more stable state for the subsoil with geostatic stress before cyclic moving loading.

In addition, neglecting the geostatic stress state leads to a significant underestimation of the shakedown limit load (Costa, Lopes, and Cardoso 2018). Larger Poisson ratios results in a higher shakedown limit, meaning this trend is clearer for higher Poisson's ratios. Thus, the shakedown limit ratio of considering geostatic stress to neglecting geostatic stress also rises with the increase of Poisson's ratio. Taking a friction angle φ=30° as an example, the ratio of the shakedown limit increases from 1.81 to 8.54 as the Poisson's ratio varies from 0.3 to 0.5 in the case of continuous slab loading.

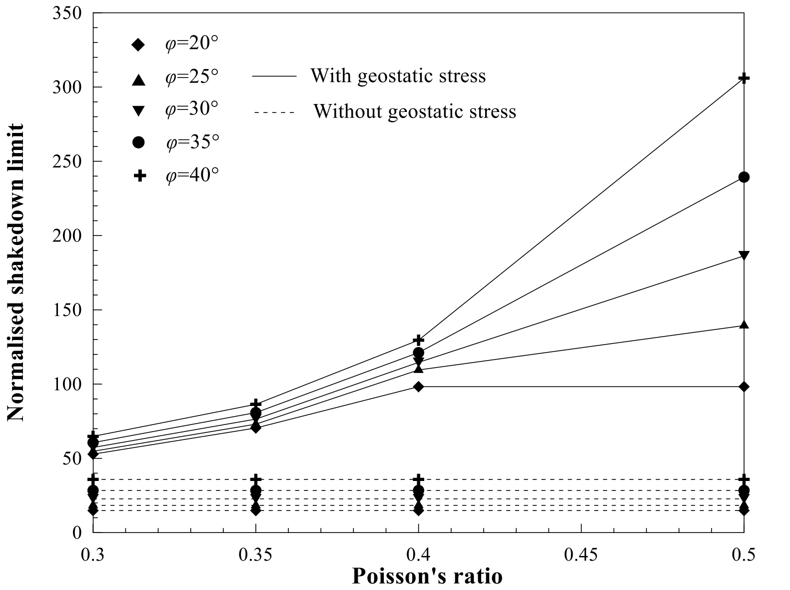

Figure 19. Normalised shakedown limit of continuous slab loading for varying Poisson's ratios

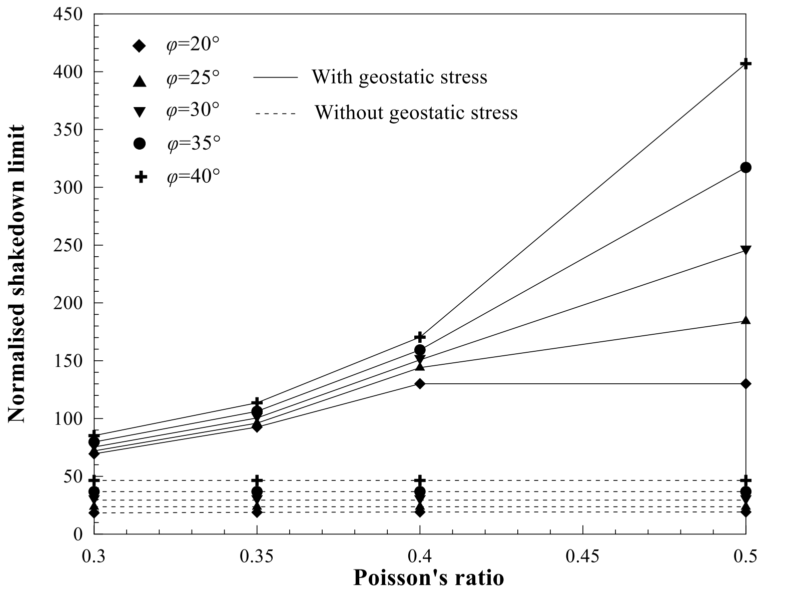

Figure 20. Normalised shakedown limit of expansion joint loading versus Poisson's ratio

5.4 Implications for track design

Based on Eqs. (9) and (10), the magnitudes of the expansion joint loading, σ'_v, and continuous slab loading σ_v, induced by a dual-axle load P_0 differ, with σ'_v being greater than σ_v. Consequently, to design a slab track foundation, the normalized shakedown limit must be converted to the corresponding axle load P_0. The shakedown axle load limits for the continuous slab loading and expansion joint loading cases are defined by Eqs. (30) and (31), respectively.

$$\left(\lambda P_0\right)_{trapzoid} = \lambda \frac{b(Z+L)\sigma_v}{4\varphi_k} \tag{30}$$

$$(\lambda P_0)_{triangular} = \lambda \frac{bZ'\sigma_v' C_0}{4\varphi_k C_v} \tag{31}$$

where C_v represents the ratio of stress levels at the expansion joints to those at continuous positions, and it is dependent on the operating speed. The correlation between the factor C_v and speed on the roadbed is illustrated in Figure 21.

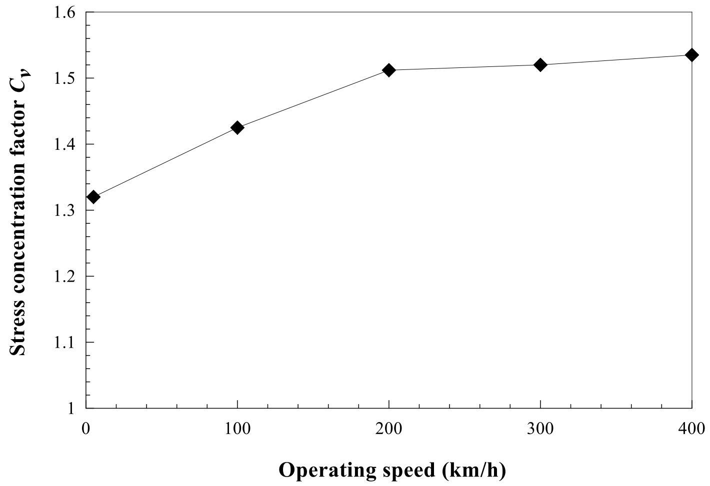

Figure 21. Stress concentration factor versus operating speed

Assuming Poisson's ratio $\mu = 0.3$ and cohesion $c = 1$ kPa, Figure 22 shows how operating speed affects the shakedown limit at different friction angles. The figure illustrates that the shakedown limit for expansion joint loading remains lower than that for continuous slab loading at the same friction angle. Therefore, for the design of the slab track foundation, the shakedown solution should fall within the range of loading between expansion joint loading and continuous slab loading, represented by the shaded region in the cases of φ=20° and 40°.

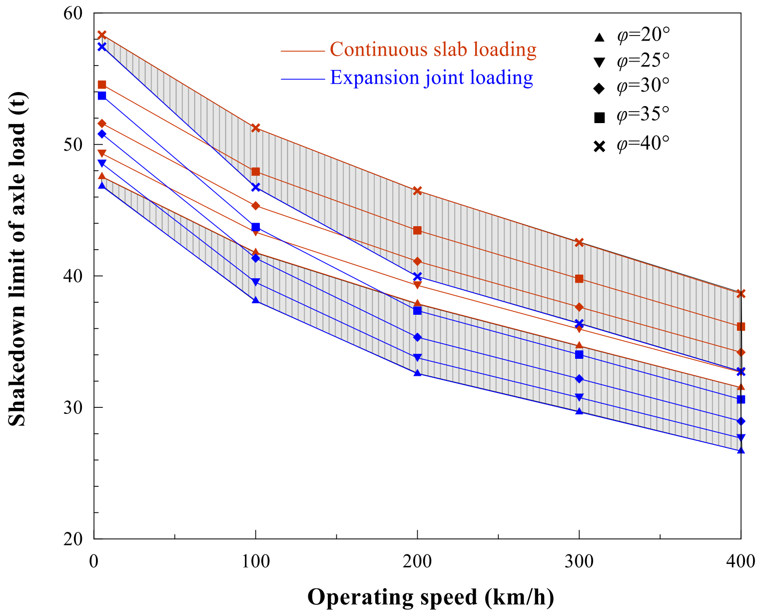

Figure 22. Shakedown limit of equivalent axle load versus operating speed: shaded areas are bounded by expansion joint loading and continuous slab loading scenarios and only presented for $\varphi = 20°$ and $40°$

When designing slab trackbed to meet the serviceability limit state (SLS), it is essential that the substructure exhibits fully elastic behavior, devoid of residual strain accumulation or approximate elastic behavior that returns to an elastic state after multiple loading cycles. The shakedown solution is responsible for determining the elastic limit beyond which the structure undergoes plastic deformation. If the load magnitude exceeds the elastic shakedown limit, plastic strains develop repeatedly, leading to failure at a low number of cycles. Consequently, the elastic shakedown limit is a significant determinant of the ultimate limit state (ULS) of slab track foundations. If the load magnitude falls below the elastic shakedown limit but exceeds the elastic limit, the subsoil response returns to its elastic state following residual stress buildup. However, the time required for residual stress buildup and cyclic settlement is not factored into the lower-bound theorem. Thus, it is necessary to adjust the shakedown limit by a factor that bridges the SLS and ULS in track design. One possible approach to determine this factor is by relating it to the cyclic settlement behavior and design requirements of the track substructure. Establishing this relationship would require extensive numerical simulations and field evidence.

6. Conclusions

This paper develops shakedown solutions for slab track substructures using lower-bound shakedown theorems. The continuous slab loading and expansion joint loading are adopted representing trackbed stress pattern when double-axle loads acting on the track's general location and joints. Analytical lower-bound shakedown solutions were established for the homogeneous half-space under two typical stress patterns and extended to shakedown analysis of slab track substructures. Shakedown analysis was incorporated into design to determine lower and upper bounds of axle load with differing operating speeds.

The parametric analysis results indicate that the presence of a geostatic stress field can effectively enhance the normalized shakedown limit under both load types with the same friction angle and Poisson's ratio. Neglecting the geostatic stress state leads to an increase in shakedown limits with increasing friction angles, which are proportional to the cohesion normalized by its value. Poisson's ratio has a minimal effect on the shakedown limit and critical depth, with the critical depth closer to the surface at depths ranging from 1.0-1.5 m and decreasing with increasing friction angles. However, considering the geostatic stress state results in a non-proportional relationship between shakedown limit and cohesion. In such cases, the geostatic stress state can lead to a significant raise-up of the shakedown limit load, particularly for higher Poisson's ratios. Moreover, the growth ratio of the shakedown limit also increases with an increasing Poisson's ratio. Therefore, the geostatic stress state cannot be neglected in railway engineering.

On the roadbed surface of the slab track structure, two loading modes exist for both continuous and joint positions. The magnitude of expansion joint loading is greater than that of continuous slab loading for the same axle load, and the magnitude ratio of expansion joint loading to continuous slab loading C_v increases with increasing train speeds. The shakedown limit of axle load reflects the influence of operating speed on the stress concentration factor C_v and dynamic amplification factor φ_k. In the design of slab trackbed, the shakedown solution for the slab track structure should be between the lower and upper bounds of continuous slab loading and expansion joint loading. The findings provide a reference for optimized design of slab substructure.

Acknowledgments

The study was supported by the National Natural Science Foundation of China under grant number 52078435, the Royal Society under grant number IEC\NSFC\211306 (International Exchanges 2021 Cost Share), the Leveulme Trust under grant number PLP-2016-270, the Natural Science Foundation of Sichuan Province under grant numbers 2022NSFSC0404 and 2023NSFSC0391, and the 111 Project under grant number B21011.

Appendix A

Tables A1, A2, A3, and A4 present the normalized shakedown limit and critical depth calculation results for continuous slab loading and expansion joint loadings with c = 1 kPa, varying in μ values.

Table A1. Normalized shakedown limit and critical depth with c=1 kPa, μ = 0.3

Friction angle	Shakedown limit of CSL		Critical depth of CSL		Shakedown limit of EJL		Critical depth of EJL	
	Without GS	With GS	Without GS	With GS	Without GS	With GS	Without GS	With GS
20°	14.85	52.81	1.37	0.00	18.37	69.45	1.47	0.00
25°	18.33	54.76	1.31	0.00	23.69	72.01	1.36	0.00
30°	22.72	57.30	1.24	0.00	29.41	75.35	1.28	0.00
35°	28.37	60.58	1.17	0.00	36.77	79.67	1.19	0.00
40°	35.81	64.78	1.05	0.00	46.45	85.19	1.11	0.00

Note: CSL, continuous slab loading; EJL, expansion joint loading; GS, geostatic stress.

Table A2. Normalized shakedown limit and critical depth with c=1 kPa, μ = 0.35

Friction angle	Shakedown limit of CSL		Critical depth of CSL		Shakedown limit of EJL		Critical depth of EJL	
	Without GS	With GS	Without GS	With GS	Without GS	With GS	Without GS	With GS
20°	14.85	70.41	1.37	0.00	18.87	92.60	1.48	0.00
25°	18.33	73.01	1.31	0.00	23.69	96.01	1.36	0.00
30°	22.72	76.40	1.24	0.00	29.41	100.47	1.28	0.00
35°	28.37	80.77	1.17	0.00	36.77	106.22	1.19	0.00
40°	35.81	86.37	1.05	0.00	46.45	113.59	1.11	0.00

Note: CSL, continuous slab loading; EJL, expansion joint loading; GS, geostatic stress.

Table A3. Normalized shakedown limit and critical depth with c=1 kPa, μ = 0.4

Friction angle	Shakedown limit of CSL		Critical depth of CSL		Shakedown limit of EJL		Critical depth of EJL	
	Without GS	With GS	Without GS	With GS	Without GS	With GS	Without GS	With GS
20°	14.85	98.26	1.37	0.39	19.14	130.10	1.44	0.40
25°	18.33	109.51	1.31	0.00	23.69	144.01	1.36	0.00
30°	22.72	114.60	1.24	0.00	29.41	150.71	1.28	0.00
35°	28.37	121.16	1.17	0.00	36.77	159.33	1.19	0.00
40°	35.81	129.56	1.05	0.00	46.45	170.38	1.11	0.00

Note: CSL, continuous slab loading; EJL, expansion joint loading; GS, geostatic stress.

Table A4. Normalized shakedown limit and critical depth with c=1 kPa, μ = 0.49

Friction angle	Shakedown limit of CSL		Critical depth of CSL		Shakedown limit of EJL		Critical depth of EJL	
	Without GS	With GS	Without GS	With GS	Without GS	With GS	Without GS	With GS
20°	14.85	98.26	1.37	0.39	19.16	130.10	1.42	0.40
25°	18.33	139.60	1.31	0.33	23.70	184.28	1.36	0.34
30°	22.72	189.47	1.24	0.22	29.41	250.97	1.28	0.21
35°	28.37	247.97	1.17	0.17	36.77	328.34	1.19	0.16
40°	35.81	321.70	1.05	0.13	46.45	426.77	1.11	0.14

Note: CSL, continuous slab loading; EJL, expansion joint loading; GS, geostatic stress.

References

Bi, Z.Q., Ye, Y.S., Gong, Q.M., Cai, D.G., Yan, H.Y., Wei, S.W., Yao J.K., 2022. An Improved Thermo-Parameters Method for Dynamic Shakedown Analysis of Railway Subgrade. Transp Geotech. 33, 100657. https://doi.org/10.1016/j.trgeo.2021.100657.

Bleich, H., 1932. Über Die Bemessung Statisch Unbestimmter Stahltragwerke Unter Berücksichtigung Des Elastisch-Plastischen Verhaltens Des Baustoffes. Bauingenieur 13, 261-269.

Boulbibane, M., Weichert, D., 1997. Application of shakedown theory to soils with non associated flow rules. Mech Res Commun. 24, 513–519.

Boussinesq, J., 1885. Applications Des Potentials à l'étude de l'équilibre et Du Mouvement Des Solidesélastiques.

Charoenwong, C., Connolly D.P., Colaco, A., Costa, P.A., Woodward, P.K., Romero, A., Galvín, P., 2023. Railway Slab vs Ballasted Track: A Comparison of Track Geometry Degradation. Constr Build Mater. 378, 131121. https://doi.org/10.1016/j.conbuildmat.2023.131121.

Charoenwong, C., Connolly D.P., Odolinski, K., Costa, P.A., Galvín, P., Smith, A., 2022. The Effect of Rolling Stock Characteristics on Differential Railway Track Settlement: An Engineering-Economic Model. Transp Geotech. 37, 100845. https://doi.org/10.1016/j.trgeo.2022.100845.

Charoenwong, C., Connolly D.P., Woodward, P.K., Galvín, P., Costa, P.A., 2022. Analytical Forecasting of Long-Term Railway Track Settlement. Comput Geotech. 143, 104601. https://doi.org/10.1016/j.compgeo.2021.104601.

Collins, I.F., Boulbibane, M., 2000. Geomechanical analysis of unbound pavements based on shakedown theory. J Geotech Geoenviron. 126, 50–59. https://doi.org/10.1061/(ASCE)1090-0241(2000)126:1(50).

Collins, I.F., Cliffe, P.F., 1987. Shakedown in frictional materials under moving surface loads. Numer Analyt Meth Geomech. 11, 409–420. https://doi.org/10.1002/nag.1610110408.

Collins, I.F., Wang, A.P., Saunders, L.R., 1993. Shakedown in layered pavements under moving surface loads. Numer Analyt Meth Geomech. 17, 165–174. https://doi.org/10.1002/nag.1610170303.

Connolly, D.P., Dong, K., Alves Costa, P., Soares, P., Woodward, P.K., 2020. High speed railway ground dynamics: a multi-model analysis. Int. J. Rail Transp. 8(4), 324–346. https://doi.org/10.1080/23248378.2020.1712267.

Connolly, D.P., Yu, H.S., 2020. A Shakedown Limit Calculation Method for Geogrid Reinforced Soils under Moving Loads. Geotext Geomembranes, 49, 688-696. https://doi.org/10.1016/j.geotexmem.2020.11.009.

Costa, P.A., Lopes, P., Cardoso, A.S., 2018. Soil Shakedown Analysis of Slab Railway Tracks: Numerical Approach and Parametric Study. Transp. Geotech. 16, 85–96. https://doi.org/10.1016/j.trgeo.2018.07.004.

Koiter W.T., 1960. General theorems for elastic-plastic solids, in: Sneddon I.N., Hill R. (Eds.), Progress of Solid Mechanics, pp. 167-221.

Krabbenhøft, K., Lyamin, A.V., Sloan, S.W., 2007. Shakedown of a cohesive-frictional half-space subjected to rolling and sliding contact. Int J Solids Struct. 44, 3998–4008. https://doi.org/10.1016/j.ijsolstr.2006.11.001.

Liu, S., Wang, J., Yu, H.S., Wanatowski, D., 2018. Shakedown for slab track substructures with stiffness variation. Geotech Res. 5, 31–38. https://doi.org/10.1680/jgere.17.00018.

Melan E., 1938. Der spannungsgudstand eines Henky-Mises schen Kontinuums bei Verlandicher Belastung. Sitzungberichte der Ak Wissenschaften Wien (Ser 2A). 147, 73.

Ponter, A.R.S., Hearle, A.D., Johnson, K.L., 1985. Application of the kinematical shakedown theorem to rolling and sliding point contacts. J Mech Phys Solids. 33, 339–362. https://doi.org/10.1016/0022-5096(85)90033-X.

Raad, L., Weichert, D., Najm, W., 1988. Stability of multilayer systems under repeated loads. Transp Res Board. 1207, 181–186.

Radovsky, B.S., Murashina, N.V., 1996. Shakedown of subgrade soil under repeated loading. Transp Res Rec. 82–88. https://doi.org/10.1177/0361198196154700112.

Sharp, R.W., Booker, J.R., 1984. Shakedown of pavements under moving surface loads. J Transp Eng. 110, 1–14. https://doi.org/10.1061/(ASCE)0733-947X(1984)110:1(1).
Wang, J., Yu, H.S., 2014. Three-dimensional shakedown solutions for anisotropic cohesive-frictional materials under moving surface loads. Numer Analyt Meth Geomech. 38, 331–348. https://doi.org/10.1002/nag.2207.
Wang, J., Liu, S., Yang, W., 2018. Dynamics shakedown analysis of slab track substructures with reference to critical speed. Soil Dyn Ear Eng. 106, 1–13. https://doi.org/10.1016/j.soildyn.2017.12.004.
Wang, J., Yu, H.S., 2013a. Shakedown analysis for design of flexible pavements under moving loads. Road Mater Pavements Des. 14, 703–722. https://doi.org/10.1080/14680629.2013.814318.
Wang, J., Yu, H.S., 2021. Shakedown Analysis and Its Application in Pavement and Railway Engineering. Comput Geotech 138, 104281. https://doi.org/10.1016/j.compgeo.2021.104281.
Wang, J., Yu, H.S., 2013b. Residual stresses and shakedown in cohesive-frictional half-space under moving surface loads. Geomech Geoengin. 8, 1–14. https://doi.org/10.1080/17486025.2012.759281.
Wang, K.Y., Zhuang, Y., 2021. Characterizing the Permanent Deformation Response-Behavior of Subgrade Material under Cyclic Loading Based on the Shakedown Theory. Constr Build Mater. 311, 125325. https://doi.org/10.1016/j.conbuildmat.2021.125325.
Wang, K.Y., Zhuang, Y., Kouretzis, G., Sloan, S.W., 2020. Shakedown Analysis of Ballasted Track Structure Using Three-Dimensional Finite Element Techniques. Acta. Geotech. 15(5), 1231–41. https://doi.org/10.1007/s11440-019-00818-6.
Wang, T., Luo, Q., Liu, J., Liu, G., Xie, H., 2020b. Method for slab track substructure design at a speed of 400 km/h. Transp Geotech. 24. https://doi.org/10.1016/j.trgeo.2020.100391.
Ye, Q.Z., Luo, Q., Feng, G.S., Wang, T., Xie, H., 2023. Stress Distribution in Roadbeds of Slab Tracks with Longitudinal Discontinuities. Railway Eng Sci. 31(1), 61–74. https://doi.org/10.1007/s40534-022-00287-w.
Yu, H.S., Hossain, M.Z., 1998. Lower bound shakedown analysis of layered pavements discontinuous stress fields. Comput Methods Appl Mech Eng. 167, 209–222. https://doi.org/10.1016/S0045-7825(98)00120-0.
Yu, H.S., Wang, J., 2012. Three-dimensional shakedown solutions for cohesive-frictional materials under moving surface loads. Int J Solids Struct. 49, 3797–3807. https://doi.org/10.1016/j.ijsolstr.2012.08.011.
Yu, H.S., 2005. Three-dimensional analytical solutions for shakedown of cohesive frictional materials under moving surface loads. Proc R Soc A. 461, 1951–1964. https://doi.org/10.1098/rspa.2005.1445.
Zhao, J.D., Sloan, S.W., Lyamin, A.V., Krabbenhøft, K., 2008. Bounds for shakedown of cohesive-frictional materials under moving surface loads. Int J Solids Struct. 45, 3290–3312. https://doi.org/10.1016/j.ijsolstr.2008.01.030.
Zhuang, Y., Wang, K.Y., Li, H.X., 2020. Shakedown Solutions for Ballasted Track Structure under Multiple Uniform Loads. Transp Geotech. 22, 100298. https://doi.org/10.1016/j.trgeo.2019.100298.
Zhuang, Y., Wang, K.Y., 2018. Shakedown Solutions for Pavement Structures with von Mises Criterion Subjected to Hertz Loads. Road Mater Pavement.19(3), 710–726. https://doi.org/10.1080/14680629.2017.1301265.
Zhuang, Y., Wang, K.Y., Li, H.X., Wang, M., Chen, L., 2019. Application of three-dimensional shakedown solutions in railway structure under multiple Hertz loads. Soil Dyn Ear Eng. 117, 328–338. https://doi.org/10.1016/j.soildyn.2018.11.031.